Research Square

Preprints are preliminary reports that have not undergone peer review.
They should not be considered conclusive, used to inform clinical practice,
or referenced by the media as validated information.

Transient thermoviscoelastic stresses in AISI 4340 steel cylinders: fractional-memory modeling, experimental benchmarking and design implications

Magdy A. Ezzat
Alexandria University
Mohamed H. Hendy
hendy442003@yahoo.com

Northern Border University
Shereen M. Ezzat
Boynton Beach,

Research Article

Keywords: AISI 4340 steel, thermal stress design, experimental benchmarking, Green–Naghdi theory, memory-dependent derivative, state-space approach

Posted Date: November 17th, 2026

DOI: https://doi.org/10.21203/rs.3.rs-11627744/v1

License: This work is licensed under a Creative Commons Attribution 4.0 International License.
Read Full License

Additional Declarations: No competing interests reported.

Transient thermoviscoelastic stresses in AISI 4340 steel cylinders: fractional-memory modeling, experimental benchmarking and design implications

Magdy A. Ezzat[1], Mohamed H. Hendy[*2] and Shereen M. Ezzat[3]

[1] *Department of Mathematics, Faculty of Education, Alexandria University, Alexandria, Egypt*

[2] *Department of General Courses, Faculty of Applied, Northern Border University, Arar, Saudi Arabia*

[3] *Independent Researcher, Boynton Beach, Florida, USA*

Abstract

The fractional heat equation of Hendy et al. (2019) is replaced by a fractional Green–Naghdi heat transport law with a memory-dependent derivative, whose fractional order is bounded by a harmonic passivity condition. The model is applied to a finite solid cylinder of AISI 4340 alloy steel, heated over a central disk of its top face and clamped at its base. Laplace transformation and a finite Hankel series reduce the problem to a two-point boundary-value problem, solved analytically by the state-space approach with growing and decaying axial modes, so that base reflections are represented. The solution is verified against independent finite-difference solutions, Chebyshev collocation, convergence tests and an exact quasi-static solution for a 20 mm cylinder. In an experimental benchmarking against published measurements on AISI 4340, the predicted thermoelastic coefficient, −1.01 K/GPa, agrees with the measured release heating, −1.2 ± 0.3 K/GPa, and the predicted longitudinal wave speed differs from the measured ultrasonic velocity by 3.7%. The tensile-bar data exclude the illustrative fractional-memory parameters at the structural scale and bound the memory time from below, but a calibration–validation test shows that they cannot identify it. For design, the allowable temperature rise under slow heating is 135–331 K across the yield-strength range of the steel. Rapid heating of short cylinders over a large part of the end face amplifies the peak von Mises stress by up to a factor of two and can make the clamped base critical, while the heat-transport law changes the peak by up to 29%.

Keywords: AISI 4340 steel; thermal stress design; experimental benchmarking; Green–Naghdi theory; memory-dependent derivative; state-space approach

[*]Corresponding author, E-mail: hendy442003@yahoo.com

1 Introduction

Alloy steels such as AISI 4340 are widely used for shafts, rotors, landing-gear members and pressure vessels, and steel is the load-bearing phase of many steel–concrete and steel–polymer composite members. Such components are often exposed to sudden, spatially localized heating, and the resulting transient thermal stresses are of direct structural interest. Predicting them requires a theory that couples deformation and heat transport consistently.

The coupled dynamical theory of thermoelasticity of Biot (1956) removed the paradox of the uncoupled theory, in which elastic deformation does not affect temperature, but it rests on Fourier's law and therefore predicts an infinite speed of thermal signals. Generalized theories were built to remove this feature. Lord and Shulman (1967) introduced a relaxation time in the heat-flux law, and Green and Lindsay (1972) introduced two relaxation times in the constitutive relations. Green and Naghdi (1991, 1992, 1993) reformulated the thermomechanics of deformable continua and obtained three linear theories: type I coincides with the classical theory, type II supports undamped thermal waves without energy dissipation, and type III contains both as special cases. A review is given by Chandrasekharaiah (1998).

Many engineering materials are viscoelastic, so that their stress depends on the strain history through a relaxation function (Gross 1953; Tschoegl 1997). Uniqueness and reciprocity theorems for generalized thermoviscoelasticity were proved by Ezzat and El-Karamany (2002, 2003), discontinuities were studied by El-Karamany and Ezzat (2004), and the state-space approach was applied to generalized thermoviscoelastic problems by Ezzat et al. (2001, 2002). Further results were reported by Sherief et al. (2015) and Hendy et al. (2018).

Fractional calculus has been used to describe anomalous heat transport and hereditary material behavior. Povstenko (2005) derived the time-fractional heat conduction equation and the associated thermal stresses, Youssef (2010) and Sherief et al. (2010) formulated fractional generalized thermoelasticity, and Ezzat (2011) introduced a fractional heat law based on a Taylor–Riemann expansion. Ezzat and El-Karamany (2012) and Ezzat et al. (2015) extended the fractional formulation to viscoelastic media. Further problems of fractional thermoelasticity were solved by Lata et al. (2016), Abbas and Kumar (2016) and Ezzat and El-Bary (2017). Wang and Li (2011) introduced the memory-dependent derivative (MDD), defined as an integral over a sliding interval with a chosen kernel, and Yu et al. (2014), Ezzat et al. (2014, 2016) and Aldawody et al. (2018) built generalized thermoelastic and thermoviscoelastic models on it.

Hendy et al. (2019) developed a fractional model of thermoviscoelasticity and solved a two-dimensional half-space problem by the state-space approach. The present work replaces their fractional heat equation, Eq. (9) of Hendy et

al. (2019), by a fractional Green–Naghdi heat transport law with a memory-dependent derivative (FMDD). Neither the memory-dependent derivative nor the cylindrical geometry is new in itself. The contribution of this study lies in (i) a finite-height axisymmetric state-space formulation that retains both growing and decaying axial modes and therefore represents stress waves reflected from a clamped base, (ii) the treatment of localized heating over a central disk with a sensitivity study of the heated edge, (iii) a passivity restriction on the fractional order of the heat law, (iv) independent numerical checks of the fractional, memory-dependent and two-dimensional parts of the solution, and (v) an experimental benchmarking against published measurements on AISI 4340 steel, namely the isentropic thermoelastic effect measured in tensile bars (Burns et al. 2025) and the measured ultrasonic wave speed. This benchmarking tests the thermoelastic coupling and the elastic wave speed of the model, examines whether the fractional-memory parameters can be identified from the data, and states the physical limitations of the model. Experimental benchmarking, numerical verification and theoretical predictions are distinguished throughout (Table 12). Finally, (vi) the results are interpreted for design in terms of the peak von Mises stress, its location and the allowable temperature rise of AISI 4340 components (Section 11). Table 1 summarizes how the present study differs from Hendy et al. (2019). The constants of AISI 4340 alloy steel (SAE 2009; MakeItFrom.com 2026) are used throughout, and the results are presented in nondimensional form whose physical scales are discussed in Section 9.2.

Table 1 Comparison of the present study with the earlier half-space study

Feature	Hendy et al. (2019)	Present study
Heat transport law	Fractional heat equation with relaxation times	Fractional Green–Naghdi law with MDD
Geometry	Half-space, plane strain	Finite solid cylinder, axisymmetric
Constraints	Semi-infinite, traction-free surface	Clamped base; restrained, insulated lateral face
Transforms	Laplace–Fourier	Laplace–finite Hankel (Dini)
Axial modes	Decaying only	Decaying and growing (reflections)
Material constants	Polymethyl methacrylate	AISI 4340 alloy steel
Passivity restriction	Not considered	Kernel-dependent bound on the fractional order
Independent checks	Comparison of limiting theories	Time-domain finite differences, collocation, convergence
Experimental benchmarking	None	Thermoelastic effect and wave speed measured for AISI 4340; identifiability of the memory parameters
Design interpretation	None	Peak von Mises stress, dynamic amplification and allowable temperature rise

The state-space method (Bahar and Hetnarski 1978; Sherief 1993; Ezzat 2008) applies to every system that integral transforms can treat and to many for which they fail. Combined here with the Laplace transform and a Dini series in the radial direction, it gives an analytical solution in the transform domain; the time-domain fields are then obtained numerically by the Fourier-series inversion of Honig and Hirdes (1984).

2 Basic equations

We consider a homogeneous, isotropic thermoviscoelastic solid. In the absence of body forces and heat sources the governing equations are as follows.

Equation of motion

$$\sigma_{ji,j} = \rho\, \ddot{u}_i. \tag{1}$$

Deviatoric constitutive equation. The stress deviator S_{ij} and strain deviator e_{ij} are related by

$$S_{ij}(\mathbf{x},t) = \int_0^t \hat{R}(t-\xi)\, \frac{\partial e_{ij}(\mathbf{x},\xi)}{\partial \xi}\, d\xi, \tag{2}$$

where

$$\begin{aligned} S_{ij} &= \sigma_{ij} - \tfrac{1}{3}\sigma_{kk}\delta_{ij}, \qquad \varepsilon_{ij} = \tfrac{1}{2}(u_{i,j} + u_{j,i}), \\ e_{ij} &= \varepsilon_{ij} - \tfrac{1}{3} e\, \delta_{ij}, \qquad e = \varepsilon_{kk}. \end{aligned} \tag{3}$$

The relaxation modulus $\hat{R}(t)$, with $\hat{R}(\infty) > 0$, is taken in the form

$$\hat{R}(t) = 2\mu\Big[1 - A\int_0^t f(\xi)\,d\xi\Big], \qquad f(t) = e^{-bt}\,t^{a-1}, \tag{4}$$

with the empirical constants $0 < a < 1$, $b > 0$ and $0 \le A < b^a/\Gamma(a)$; the last inequality guarantees $\hat{R}(\infty) > 0$. For $A = 0$ the material is elastic.

Volumetric relation. The relaxation of the volumetric properties is neglected:

$$\tfrac{1}{3}\sigma_{kk} = K\,e - \gamma\,\theta, \qquad \gamma = 3K\alpha_T, \tag{5}$$

where $\theta = T - T_0$ with $|\theta/T_0| \ll 1$, K is the bulk modulus and α_T the coefficient of linear thermal expansion. Because the Green–Naghdi framework introduces no thermal relaxation into the constitutive relations, the operator $(1 + \frac{v^\alpha}{\alpha!}\frac{\partial^\alpha}{\partial t^\alpha})$ that multiplies θ in Eqs. (6)–(8) of Hendy et al. (2019) does not appear. Combining Eqs. (2), (3) and (5) gives

$$\begin{aligned}\sigma_{ij} = &\int_0^t \hat{R}(t-\xi)\,\frac{\partial}{\partial\xi}\Big(\varepsilon_{ij} - \frac{e}{3}\delta_{ij}\Big)d\xi \\ &+ (Ke - \gamma\theta)\delta_{ij},\end{aligned} \tag{6}$$

and substitution into Eq. (1) yields

$$\begin{aligned}\rho\,\ddot{u}_i = &\int_0^t \hat{R}(t-\xi)\,\frac{\partial}{\partial\xi}\Big(\tfrac{1}{2}\nabla^2 u_i + \tfrac{1}{6}e_{,i}\Big)d\xi \\ &+ Ke_{,i} - \gamma\,\theta_{,i}.\end{aligned} \tag{7}$$

Fractional Green–Naghdi heat equation with a memory-dependent derivative. The fractional heat equation, Eq. (9) of Hendy et al. (2019), is replaced by

$$k\,\theta_{,ii} = \tau_v^\beta\,\frac{\partial^\beta}{\partial t^\beta}(1 + \omega D_\omega)[\rho C_E\dot{\theta} + \gamma T_0\dot{e}], \tag{8}$$

with $0 < \beta \le 1$. Here k is the thermal conductivity, C_E the specific heat at constant strain, τ_v a relaxation parameter of the Green–Naghdi type and $\partial^\beta/\partial t^\beta$ the Caputo derivative,

$$\frac{\partial^\beta f}{\partial t^\beta} = \frac{1}{\Gamma(1-\beta)}\int_0^t \frac{f'(\xi)\,d\xi}{(t-\xi)^\beta}, \quad 0 < \beta < 1, \tag{9}$$

with $\partial^1 f/\partial t^1 = f'$. The memory-dependent derivative over the time-delay $\omega > 0$ is (Wang and Li 2011; Yu et al. 2014)

$$D_\omega f(t) = \frac{1}{\omega}\int_{t-\omega}^t K(t-\xi)\,f'(\xi)\,d\xi, \tag{10}$$

with the kernel

$$K(t-\xi) = 1 - \frac{2b_0}{\omega}(t-\xi) + \frac{a_0^2}{\omega^2}(t-\xi)^2, \tag{11}$$

where a_0 and b_0 are constants. Three kernels are examined: $K = 1$ ($a_0 = b_0 = 0$), $K = 1 - (t-\xi)/\omega$ ($a_0 = 0$, $b_0 = \frac{1}{2}$) and $K = (1 - (t-\xi)/\omega)^2$ ($a_0 = b_0 = 1$). For an anisotropic conductor the left-hand side of Eq. (8) is $k_{ij}\theta_{,ij}$; for the isotropic steel considered here it reduces to $k\theta_{,ii}$.

2.1 Limiting cases

Together with Eqs. (1)–(7), Eq. (8) contains the following theories:

- $\beta \to 0$, $\omega \to 0$, $A = 0$: the coupled theory of Biot (1956) (CTE);

- $\beta \to 0$, $\omega \to 0$, $A > 0$: coupled thermoviscoelasticity (Gross 1953);
- $\beta \to 0$, $K = 1$, small ω: $(1 + \omega D_\omega) f \simeq f + \omega \dot{f}$, i.e. the Lord–Shulman theory (Lord and Shulman 1967) with relaxation time ω; for finite ω, the MDD models of Yu et al. (2014) and Ezzat et al. (2014);
- $\beta = 1$, $\omega \to 0$: $k\theta_{,ii} = \tau_v(\rho C_E \ddot{\theta} + \gamma T_0 \ddot{e})$, the Green–Naghdi type II theory (Green and Naghdi 1992, 1993) with $k^* = k/\tau_v$;
- $0 < \beta < 1$, $\omega > 0$, $A \geq 0$: the present FMDD thermoviscoelastic model.

2.2 Thermal passivity restriction

The fractional order cannot be chosen freely when $\omega > 0$. For the uncoupled form of Eq. (8), a time-harmonic temperature field $\theta \propto e^{i\Omega t}$ is associated with the heat flux $\mathbf{q} = -k\,[i\Omega/\Lambda(i\Omega)]\,\nabla\theta$, where $\Lambda(s)$ is the Laplace symbol defined in Eq. (28) below. The cycle-averaged dissipation $-\mathbf{q}\cdot\nabla\theta^*$ is non-negative for every frequency only if

$$\operatorname{Re}\left\{ e^{i\pi\beta/2}\left[1 + G(i\Omega)\right]\right\} \geq 0 \quad \text{for all } \Omega > 0, \tag{12}$$

where G is given by Eq. (27). Since G depends on Ω only through $\Omega\omega$, condition (12) gives a kernel-dependent upper bound $\beta_{\max}$ that is independent of ω. For $K = 1$, $1 + G(i\Omega) = 2 - e^{-i\Omega\omega}$, and condition (12) reduces to $\cos(\pi\beta/2) \geq \tfrac{1}{2}$, i.e. $\beta \leq 2/3$. The bounds for the three kernels, computed by minimizing the left-hand side of Eq. (12) over $\Omega\omega$, are listed in Table 2.

Table 2 Upper bounds of the fractional order imposed by harmonic passivity

Kernel $K(t-\xi)$	$\beta_{\max}$
1	0.666667
$1 - (t-\xi)/\omega$	0.720953
$(1 - (t-\xi)/\omega)^2$	0.742019

All parameter sets used in the numerical study satisfy these bounds; in particular, the largest fractional order with the quadratic kernel is $\beta = 0.70$. The bounds concern the uncoupled thermal law only and do not by themselves establish stability of the complete coupled thermoviscoelastic system. For $\beta = 1$ and $\omega = 0$ the left-hand side of Eq. (12) vanishes, which reflects the non-dissipative character of the Green–Naghdi type II theory.

3 Formulation of the problem for a finite cylinder

We consider a solid circular cylinder of radius R_0 and height h (Fig. 1). Cylindrical coordinates (r, φ, z) are used, with the origin at the centre of the top face and the z-axis pointing into the cylinder. The problem is axisymmetric:

$$\mathbf{u} = (u_r, 0, u_z)(r, z, t), \qquad \theta = \theta(r, z, t), \tag{13}$$

$$e = \frac{1}{r}\frac{\partial (r u_r)}{\partial r} + \frac{\partial u_z}{\partial z}, \quad \nabla^2 = \frac{\partial^2}{\partial r^2} + \frac{1}{r}\frac{\partial}{\partial r} + \frac{\partial^2}{\partial z^2}. \tag{14}$$

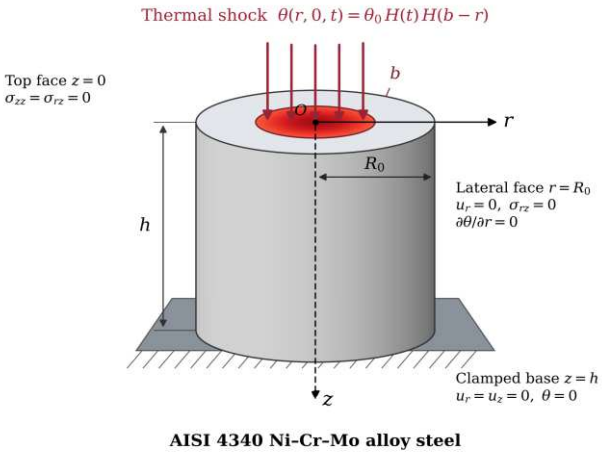


Fig. 1 Schematic of the cylinder of finite height under a thermal shock applied over a central disk of the top face

The top face $z=0$ is traction free and is suddenly heated over the disk $r \le b$. The lateral face $r=R_0$ is thermally insulated, free of shear and radially restrained (a smooth rigid sleeve). The base $z=h$ is clamped and held at the reference temperature:

$$\sigma_{zz}=\sigma_{rz}=0, \quad \theta=\theta_0 H(t)H(b-r) \quad (z=0), \tag{15}$$

$$u_r=0, \quad \sigma_{rz}=0, \quad \partial\theta/\partial r=0 \quad (r=R_0), \tag{16}$$

$$u_r=u_z=0, \quad \theta=0 \quad (z=h), \tag{17}$$

where $H(\cdot)$ is the Heaviside unit step function. The medium is initially at rest at T_0. The sensitivity of the results to the sharp edge of the heated disk is examined in Section 8.4 by replacing $H(b-r)$ with the smoothed profile $\tfrac{1}{2}[1-\tanh((r-b)/\delta)]$.

The following nondimensional variables are introduced:

$$\begin{aligned}
&(r^*, z^*, u_r^*, u_z^*, R_0^*, h^*, b^*) = c_0\eta_0\,(r, z, u_r, u_z, R_0, h, b),\\
&(t^*, \tau_v^*, \omega^*) = c_0^2\eta_0\,(t, \tau_v, \omega), \qquad b_{\mathrm{v}}^* = \frac{b}{c_0^2\eta_0},\\
&\theta^* = \frac{\gamma\,\theta}{\lambda+2\mu}, \qquad \sigma_{ij}^* = \frac{\sigma_{ij}}{\lambda+2\mu},\\
&c_0^2 = \frac{\lambda+2\mu}{\rho}, \qquad \eta_0 = \frac{\rho C_E}{k}.
\end{aligned} \tag{18}$$

Here b_{v}^* is the nondimensional decay constant of the relaxation function (4), distinguished from the heated radius b^*. Dropping the asterisks, the governing equations become

$$\ddot{u}_r = \mathcal{M}\Big[\nabla^2 u_r - \frac{u_r}{r^2}\Big] + (\kappa+\tfrac{1}{3}\mathcal{M})\frac{\partial e}{\partial r} - \frac{\partial\theta}{\partial r}, \tag{19}$$

$$\ddot{u}_z = \mathcal{M}[\nabla^2 u_z] + (\kappa+\tfrac{1}{3}\mathcal{M})\frac{\partial e}{\partial z} - \frac{\partial\theta}{\partial z}, \tag{20}$$

$$\nabla^2\theta = \tau_v^{\beta}\frac{\partial^{\beta}}{\partial t^{\beta}}(1+\omega D_{\omega})\Big[\frac{\partial\theta}{\partial t} + \varepsilon\frac{\partial e}{\partial t}\Big], \tag{21}$$

$$\begin{aligned}
\sigma_{zz} &= (\kappa-\tfrac{2}{3}\mathcal{M})[e] + 2\mathcal{M}[\partial u_z/\partial z] - \theta,\\
\sigma_{rr} &= (\kappa-\tfrac{2}{3}\mathcal{M})[e] + 2\mathcal{M}[\partial u_r/\partial r] - \theta,
\end{aligned} \tag{22}$$

$$\begin{aligned}
\sigma_{\varphi\varphi} &= (\kappa-\tfrac{2}{3}\mathcal{M})[e] + 2\mathcal{M}[u_r/r] - \theta,\\
\sigma_{rz} &= \mathcal{M}[\partial u_r/\partial z + \partial u_z/\partial r].
\end{aligned} \tag{23}$$

In Eqs. (19)–(23), $\kappa = K/(\lambda+2\mu)$, $\varepsilon = \gamma^2 T_0/[\rho C_E(\lambda+2\mu)]$ is the thermoelastic coupling parameter, and $\mathcal{M}$ is the hereditary operator

$$\mathcal{M}[g] = \hat{\mu}\int_0^t \Big[1 - A\int_0^{t-\xi} e^{-b_{\mathrm{v}}\eta}\eta^{a-1}d\eta\Big]\frac{\partial g}{\partial\xi}\,d\xi, \tag{24}$$

with $\hat{\mu}=\mu/(\lambda+2\mu)$. Because the problem is linear, every field is proportional to the nondimensional surface temperature θ_0; all results are therefore reported per unit θ_0, i.e. as θ/θ_0, u/θ_0 and σ/θ_0. In dimensional terms $\sigma/\theta_0 = \sigma_{\mathrm{phys}}/(\gamma\,\Delta T_0)$, where ΔT_0 is the applied temperature rise.

4 Laplace transform and finite Hankel series

The Laplace transform of $g(r,z,t)$ is

$$\bar{g}(r,z,s)=\int_0^\infty e^{-st}g(r,z,t)\,dt. \tag{25}$$

For homogeneous initial conditions $\mathcal{M}$ becomes multiplication by

$$\mu^*(s)=\hat{\mu}\Big[1-\frac{A\,\Gamma(a)}{(s+b_{\mathrm{v}})^a}\Big], \tag{26}$$

so that the transformed equations are those of an elastic solid with s-dependent moduli $\mu^*(s)$ and $\lambda^*(s)=\kappa-\frac{2}{3}\mu^*(s)$; the longitudinal modulus is $D_L(s)=\kappa+\frac{4}{3}\mu^*(s)$, which equals 1 in the elastic case. With $\mathcal{L}\{\partial^\beta f/\partial t^\beta\}=s^\beta\bar{f}$ and $\mathcal{L}\{\omega D_\omega f\}=G(s)\bar{f}$,

$$\begin{aligned}G(s)=&(1-e^{-s\omega})\Big(1-\frac{2b_0}{\omega s}+\frac{2a_0^2}{\omega^2 s^2}\Big)\\&-\Big(a_0^2-2b_0+\frac{2a_0^2}{\omega s}\Big)e^{-s\omega}.\end{aligned} \tag{27}$$

Eq. (21) therefore becomes

$$\nabla^2\bar{\theta}=\Lambda(s)\,(\bar{\theta}+\varepsilon\bar{e}),\quad \Lambda(s)=\tau_v^\beta s^{\beta+1}[1+G(s)]. \tag{28}$$

The function $\Lambda(s)$ carries the whole heat transport law: $\Lambda=s$ for Biot, $\Lambda=s+\omega s^2$ for Lord–Shulman and $\Lambda=\tau_v s^2$ for Green–Naghdi II.

The displacement is written in terms of a scalar potential ϕ and the azimuthal component ψ of a vector potential:

$$u_r=\frac{\partial\phi}{\partial r}-\frac{\partial\psi}{\partial z},\quad u_z=\frac{\partial\phi}{\partial z}+\frac{1}{r}\frac{\partial(r\psi)}{\partial r},\quad e=\nabla^2\phi. \tag{29}$$

Substituting Eq. (29) into the transformed Eqs. (19) and (20) gives

$$D_L\nabla^2\bar{\phi}-s^2\bar{\phi}=\bar{\theta},\qquad \mu^*(\nabla^2-r^{-2})\bar{\psi}=s^2\bar{\psi}. \tag{30}$$

The lateral conditions (16) are satisfied exactly by the Dini series

$$\begin{aligned}\{\bar{\phi},\bar{\theta},\bar{e}\}&=\sum_{n=0}^{\infty}\{\bar{\phi}_n,\bar{\theta}_n,\bar{e}_n\}(z,s)\,J_0(\xi_n r),\\ \bar{\psi}&=\sum_{n=1}^{\infty}\bar{\psi}_n(z,s)\,J_1(\xi_n r),\end{aligned} \tag{31}$$

where $\xi_0=0$ and $\xi_n\ \ (n\ge 1)$ are the positive roots of $J_1(\xi_n R_0)=0$. Since $\partial J_0(\xi r)/\partial r=-\xi J_1(\xi r)$, the radial displacement, shear stress and radial heat flux are proportional to $J_1(\xi_n r)$ and vanish at $r=R_0$. For the sharp-edged heating the Dini coefficients of the surface temperature are

$$f_0=\frac{b^2}{R_0^2},\qquad f_n=\frac{2b\,J_1(\xi_n b)}{\xi_n R_0^2\,J_0^2(\xi_n R_0)}\ \ (n\ge 1); \tag{32}$$

for the smoothed profile they are evaluated by numerical quadrature.

5 State-space approach

For each mode, $\nabla^2\to D^2-\xi^2$ with $D=d/dz$. Eliminating $\bar{\phi}$ between Eqs. (28) and (30) gives

$$D^2\bar{e}_n=L_1\bar{e}_n+L_2\bar{\theta}_n,\qquad D^2\bar{\theta}_n=M_1\bar{e}_n+M_2\bar{\theta}_n, \tag{33}$$

$$L_1=\xi^2+\frac{s^2+\varepsilon\Lambda}{D_L},\ L_2=\frac{\Lambda}{D_L},\ M_1=\varepsilon\Lambda,\ M_2=\xi^2+\Lambda. \tag{34}$$

With $\bar{e}_n$ and $\bar{\theta}_n$ as state variables,

$$\frac{d^2\mathbf{V}}{dz^2} = \mathbf{A}\,\mathbf{V}, \quad \mathbf{V} = \begin{bmatrix} \bar{e}_n \\ \bar{\theta}_n \end{bmatrix}, \quad \mathbf{A} = \begin{bmatrix} L_1 & L_2 \\ M_1 & M_2 \end{bmatrix}. \tag{35}$$

Because the cylinder has a finite height, both exponential branches are retained:

$$\mathbf{V}(z) = e^{-\sqrt{\mathbf{A}}\,z}\,\mathbf{C}_1 + e^{-\sqrt{\mathbf{A}}\,(h-z)}\,\mathbf{C}_2, \tag{36}$$

where $\mathbf{C}_1$ and $\mathbf{C}_2$ are constant vectors. With the branch $\operatorname{Re}\sqrt{k} > 0$, both matrix exponentials are bounded for $0 \le z \le h$, which keeps the computation free of overflow for every s and ξ_n. The characteristic equation of $\mathbf{A}$ is

$$k^2 - (L_1 + M_2)\,k + L_1 M_2 - L_2 M_1 = 0, \tag{37}$$

with roots k_1, k_2. By the Cayley–Hamilton theorem,

$$e^{-\sqrt{\mathbf{A}}\,z} = a_0(z)\,\mathbf{I} + a_1(z)\,\mathbf{A}, \tag{38}$$

$$a_0 = \frac{k_1 e^{-m_2 z} - k_2 e^{-m_1 z}}{k_1 - k_2}, \quad a_1 = \frac{e^{-m_1 z} - e^{-m_2 z}}{k_1 - k_2}, \tag{39}$$

with $m_i = \sqrt{k_i}$. The entries ℓ_{ij} of the matrix exponential are

$$\begin{aligned} \ell_{11} &= \frac{(k_1 - L_1)e^{-m_2 z} - (k_2 - L_1)e^{-m_1 z}}{k_1 - k_2}, \\ \ell_{12} &= \frac{L_2(e^{-m_1 z} - e^{-m_2 z})}{k_1 - k_2}, \\ \ell_{21} &= \frac{M_1(e^{-m_1 z} - e^{-m_2 z})}{k_1 - k_2}, \\ \ell_{22} &= \frac{(k_1 - M_2)e^{-m_2 z} - (k_2 - M_2)e^{-m_1 z}}{k_1 - k_2}. \end{aligned} \tag{40}$$

Eq. (36) is equivalent to the modal form

$$\begin{aligned} \bar{e}_n &= \textstyle\sum_{i=1}^{2} p_i[\alpha_i e^{-m_i z} + \delta_i e^{-m_i (h-z)}], \\ \bar{\theta}_n &= \textstyle\sum_{i=1}^{2} g_i[\alpha_i e^{-m_i z} + \delta_i e^{-m_i (h-z)}], \end{aligned} \tag{41}$$

where $p_i = k_i - \xi^2$ are the roots of

$$D_L p^2 - (D_L \Lambda + s^2 + \varepsilon\Lambda)p + s^2\Lambda = 0, \tag{42}$$

and $g_i = D_L p_i - s^2$. The ratio $g_i/p_i = (k_i - L_1)/L_2$ is the eigenvector of $\mathbf{A}$ belonging to k_i. The scalar potential and the shear mode are

$$\bar{\phi}_n = \textstyle\sum_{i=1}^{2} [\alpha_i e^{-m_i z} + \delta_i e^{-m_i (h-z)}], \tag{43}$$

$$\bar{\psi}_n = \alpha_3 e^{-m_3 z} + \delta_3 e^{-m_3 (h-z)}, \quad m_3 = \sqrt{\xi^2 + s^2/\mu^*}. \tag{44}$$

The Dini coefficients of the displacements and stresses are

$$\bar{u}_{r,n} = -\xi\bar{\phi}_n - D\bar{\psi}_n, \qquad \bar{u}_{z,n} = D\bar{\phi}_n + \xi\bar{\psi}_n, \tag{45}$$

$$\begin{aligned} \bar{\sigma}_{zz,n} &= \lambda^* \bar{e}_n + 2\mu^*(D^2\bar{\phi}_n + \xi D\bar{\psi}_n) - \bar{\theta}_n, \\ \bar{\sigma}_{rz,n} &= -\mu^*[2\xi D\bar{\phi}_n + (m_3^2 + \xi^2)\bar{\psi}_n], \end{aligned} \tag{46}$$

with $\bar{u}_r = \sum \bar{u}_{r,n} J_1(\xi_n r)$, $\bar{u}_z = \sum \bar{u}_{z,n} J_0(\xi_n r)$, $\bar{\sigma}_{zz} = \sum \bar{\sigma}_{zz,n} J_0(\xi_n r)$ and $\bar{\sigma}_{rz} = \sum \bar{\sigma}_{rz,n} J_1(\xi_n r)$. The radial and hoop stresses follow from Eqs. (22) and (23):

$$\begin{aligned}
\bar{\sigma}_{rr} &= \sum_n \Big\{ (\lambda^* \bar{e}_n - \bar{\theta}_n) J_0(\xi_n r) \\
&\qquad + 2\mu^* \bar{u}_{r,n} [\xi_n J_0(\xi_n r) - J_1(\xi_n r)/r] \Big\}, \\
\bar{\sigma}_{\varphi\varphi} &= \sum_n \Big\{ (\lambda^* \bar{e}_n - \bar{\theta}_n) J_0(\xi_n r) \\
&\qquad + 2\mu^* \bar{u}_{r,n} J_1(\xi_n r)/r \Big\}.
\end{aligned} \tag{47}$$

6 Boundary conditions and transform-domain solution

The six constants $\alpha_1, \alpha_2, \alpha_3, \delta_1, \delta_2, \delta_3$ of each mode follow from the transformed conditions (15) and (17):

$$\bar{\sigma}_{zz,n}(0) = 0, \quad \bar{\sigma}_{rz,n}(0) = 0, \quad \bar{\theta}_n(0) = \theta_0 f_n / s, \tag{48}$$

$$\bar{u}_{r,n}(h) = 0, \quad \bar{u}_{z,n}(h) = 0, \quad \bar{\theta}_n(h) = 0. \tag{49}$$

With $E_i = e^{-m_i h}$ and $c_i = \lambda^* p_i + 2\mu^* m_i^2 - g_i$, Eqs. (48) and (49) read

$$\begin{aligned}
&\textstyle\sum_{i=1}^{2} c_i(\alpha_i + \delta_i E_i) - 2\mu^* \xi m_3 (\alpha_3 - \delta_3 E_3) = 0, \\
&\textstyle\sum_{i=1}^{2} 2\mu^* \xi m_i (\alpha_i - \delta_i E_i) - \mu^* (m_3^2 + \xi^2)(\alpha_3 + \delta_3 E_3) = 0, \\
&\textstyle\sum_{i=1}^{2} g_i (\alpha_i + \delta_i E_i) = \theta_0 f_n / s,
\end{aligned} \tag{50}$$

$$\begin{aligned}
&-\xi \textstyle\sum_{i=1}^{2} (\alpha_i E_i + \delta_i) + m_3 (\alpha_3 E_3 - \delta_3) = 0, \\
&\textstyle\sum_{i=1}^{2} m_i (\delta_i - \alpha_i E_i) + \xi (\alpha_3 E_3 + \delta_3) = 0, \\
&\textstyle\sum_{i=1}^{2} g_i (\alpha_i E_i + \delta_i) = 0.
\end{aligned} \tag{51}$$

This 6×6 linear system is solved for each mode and each value of s required by the inversion. For $\xi_0 = 0$ the shear mode decouples and the system gives $\alpha_3 = \delta_3 = 0$, so that the $n = 0$ term reproduces the solution for a uniformly heated layer. The solution in the Laplace–Hankel domain is thus analytical; the only approximations are the numerical inversion of the Laplace transform and the truncation of the Dini series.

7 Numerical inversion

The inverse Laplace transform is evaluated by the Fourier-series method of Honig and Hirdes (1984):

$$\begin{aligned}
g(t) \approx \frac{e^{ct}}{T} \Big[&\tfrac{1}{2} \bar{g}(c) \\
&+ \textstyle\sum_{k=1}^{N} \sigma_k \, \mathrm{Re} \left\{ \bar{g}(c + ik\pi/T) \, e^{ik\pi t/T} \right\} \Big],
\end{aligned} \tag{52}$$

where c exceeds the real parts of all singularities of $\bar{g}$. We take $T = t$ and $cT = 5$, so that the discretization error is of order $e^{-2cT} \approx 5 \times 10^{-5}$. Lanczos factors $\sigma_k = \mathrm{sinc}[k/(N+1)]$ limit the Gibbs oscillations produced by the step heating and by the wave fronts, and the same factors, $\mathrm{sinc}(n/N_m)$, are applied to the Dini series truncated after N_m modes. Unless stated otherwise, $N = 500\text{–}2000$ and $N_m = 70\text{–}160$. The convergence with respect to both parameters is quantified in Section 8.3.

8 Verification

The state-space solution, the independent solvers used to check it and the benchmarking and design calculations were implemented in Python 3.13 with NumPy and SciPy. All results were checked through the independent verifications described in this section.

8.1 Limiting cases against an independent time-domain solver

When the whole top face is heated ($b = R_0$) only the $n = 0$ term survives, and the problem reduces to the one-dimensional response of a layer clamped at $z = h$ and suddenly heated at its free surface. This case was solved independently by explicit finite differences in the time domain, without any transform: central differences in z, leapfrog time stepping for the momentum equation and for the hyperbolic heat equations, and a ghost node enforcing $\sigma_{zz} = 0$ at $z = 0$. Three limiting heat laws were used: Biot ($\Lambda = s$), Lord–Shulman with $\tau_0 = 0.2$ ($\Lambda = s + 0.2s^2$) and Green–Naghdi II with $\tau_v = 0.5$ ($\Lambda = 0.5s^2$), all with $A = 0$.

8.2 Fractional, memory-dependent and viscoelastic case

The full FMDD model was checked in the same one-dimensional setting with a second, independent time-domain solver. In this solver the fractional operator is inverted as $q = \tau_v^{-\beta} I^{\beta}[\nabla^2\theta]$, where I^{β} is the Riemann–Liouville integral evaluated by product integration over the whole history. The memory-dependent derivative is rewritten, after integration by parts, as $[1 + K(0)]\dot{g} = q + K(\omega)\dot{g}(t-\omega) - \int_0^{\omega} K'(u)\,\dot{g}(t-u)\,du$ with $g = \theta + \varepsilon e$. The hereditary operator (24) is evaluated as $\mathcal{M}[g] = \hat{\mu}[g - A\int_0^t f(t-\xi)g(\xi)d\xi]$ with exact interval weights of the weakly singular kernel. Three cases were computed with the quadratic kernel and $\omega = 0.2$: $\beta = 0.25$ with $A = 0$, and $\beta = 0.5$ and $\beta = 0.70$ with $A = 0.1$.

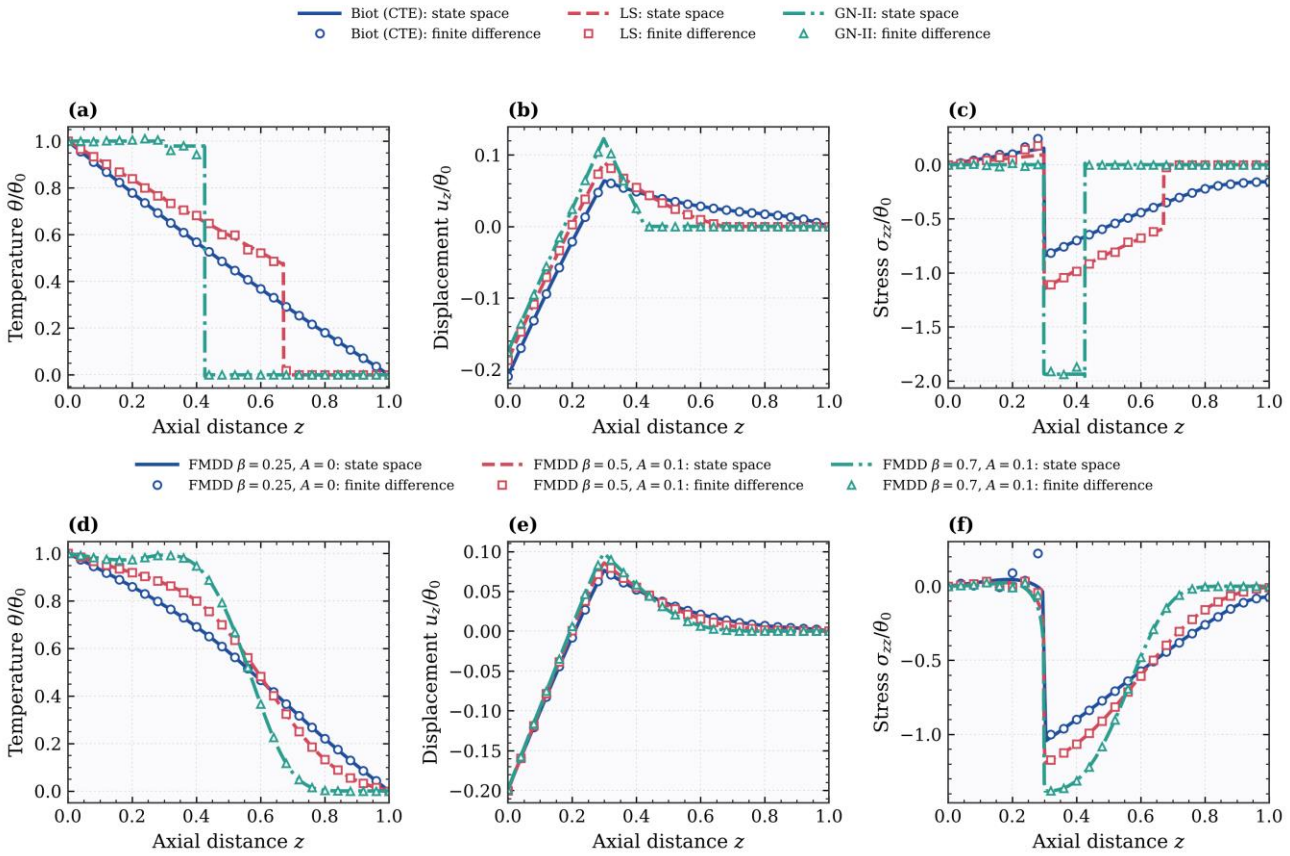


Fig. 2 Verification of the state-space solution (lines) against independent time-domain finite-difference solutions (markers) at $t = 0.3$ in the one-dimensional limit $b = R_0$: (a)–(c) limiting theories ($A = 0$); (d)–(f) FMDD model with the quadratic kernel and $\omega = 0.2$. Columns: temperature, axial displacement and axial stress

Table 3 Differences between the state-space solution and independent time-domain finite-difference solutions at $t = 0.3$ ($b = R_0$). J = number of grid intervals over $0 \le z \le 1$; RMS over all grid points; the last column excludes $|z - z_{\text{front}}| \le 0.05$

Case	J	RMS θ	RMS u_z	RMS σ_{zz}	RMS σ_{zz} (away from fronts)
Biot (CTE)	800	2.7e-05	8.3e-05	3.8e-02	1.1e-02
LS	800	2.3e-02	1.0e-04	5.7e-02	1.6e-02
GN-II	3200	2.6e-02	4.7e-05	6.9e-02	1.1e-02
FMDD, $\beta = 0.25$, $A = 0$	200	3.4e-05	3.5e-04	5.3e-02	2.1e-02
FMDD, $\beta = 0.5$, $A = 0.1$	400	2.4e-04	1.5e-04	4.1e-02	1.2e-02
FMDD, $\beta = 0.7$, $A = 0.1$	400	1.7e-04	1.6e-04	4.5e-02	1.3e-02

Fig. 2 and Table 3 show the comparison. For all six cases the root-mean-square (RMS) differences in temperature and displacement are of order 10^{-5}–10^{-3} for the grids listed, except for the temperature in the Lord–Shulman and Green–Naghdi II cases (0.023 and 0.026), where the RMS value is dominated by the thermal jump fronts. For the FMDD cases the differences decrease approximately in proportion to the grid spacing when the grid is refined (for $\beta = 0.5$, $A = 0.1$ the RMS temperature difference is 1.4e-03, 5.8e-04 and 2.4e-04 for $J = 100$, 200 and 400), which confirms that the remaining discrepancy is the truncation error of the finite-difference solver. The axial stress contains jumps at the elastic front $z = t$, and its RMS difference (0.04–0.07) is dominated by the dispersive oscillations of the finite-difference scheme there; away from the fronts ($|z - z_{\text{front}}| > 0.05$) the difference is 1.1e-02–2.1e-02.

8.3 Two-dimensional transform-domain check and convergence

The state-space solution for the modes $n \ge 1$, which carry the two-dimensional character of the problem, was checked in the transform domain against an independent Chebyshev collocation solution of the original second-order boundary-value problem for $\bar{\phi}_n$, $\bar{\theta}_n$ and $\bar{\psi}_n$ (110–260 collocation points), with the six conditions (48) and (49) imposed directly. The comparison used the default FMDD parameters with $A = 0.1$, four values of s (including those with $|s|$ up to 158 used by the inversion at $t = 0.3$) and the modes $n = 0, 1, 5, 20, 40$. The maximum relative differences in $\bar{\theta}_n$, $\bar{u}_{z,n}$ and $\bar{\sigma}_{zz,n}$ over $0 \le z \le h$ were at most 8e-10, 3e-07 and 2e-04, i.e. at the level of the collocation error.

Table 4 lists the time-domain values at four interior points for increasing N_m and N. Doubling N_m from 160 to 320 changes the values by less than 1e-04, and increasing N from 500 to 2000 by less than 1e-04. The boundary conditions are satisfied to round-off: at $t = 0.3$ the largest residuals of σ_{zz} and σ_{rz} on the top face and of u_r, u_z and θ on the clamped base are below 10^{-12} for $N_m = 40$–160.

Table 4 Convergence of time-domain values at $t = 0.3$ with the number of Dini modes N_m and of Laplace terms N (FMDD, default parameters); points are given as (r, z)

N_m	N	θ/θ_0 at (0, 0.2)	u_z/θ_0 at (0.25, 0.1)	σ_{zz}/θ_0 at (0.5, 0.4)	$\sigma_{\varphi\varphi}/\theta_0$ at (0.75, 0.2)
40	500	0.69569	-0.08414	-0.40077	-0.11883
80	500	0.69585	-0.08416	-0.40087	-0.11828
160	500	0.69589	-0.08417	-0.40089	-0.11822
320	500	0.69590	-0.08417	-0.40090	-0.11820
320	1000	0.69589	-0.08417	-0.40089	-0.11820
320	2000	0.69588	-0.08417	-0.40089	-0.11820

8.4 Sensitivity to the edge of the heated disk

Condition (15) imposes a jump of the surface temperature at $r = b$. To separate physical effects from those of this idealization and of the series truncation, the step was replaced by the smoothed profile $\frac{1}{2}[1 - \tanh((r - b)/\delta)]$ with $\delta = 0.02$ and 0.05 (Fig. 3 and Table 5). Away from the edge the fields are practically unchanged: the hoop stress on the axis of the top face varies by about 1%. The change of the hoop stress across the edge, measured between $r = 0.45$ and $r = 0.55$, converges with N_m in all three cases and decreases from 0.352 for the sharp edge to 0.348 for $\delta = 0.02$ and 0.264 for $\delta = 0.05$. In contrast, for the sharp edge the minimum axial stress at $z = 0.1$ still changes when N_m is doubled (from -0.0599 at $N_m = 160$ to -0.0609 at $N_m = 320$), which indicates a local singularity of the idealized step; for the smoothed edges it converges. Local edge stresses are therefore reported only for converged smoothed profiles, and no failure or fatigue conclusions are drawn from them.

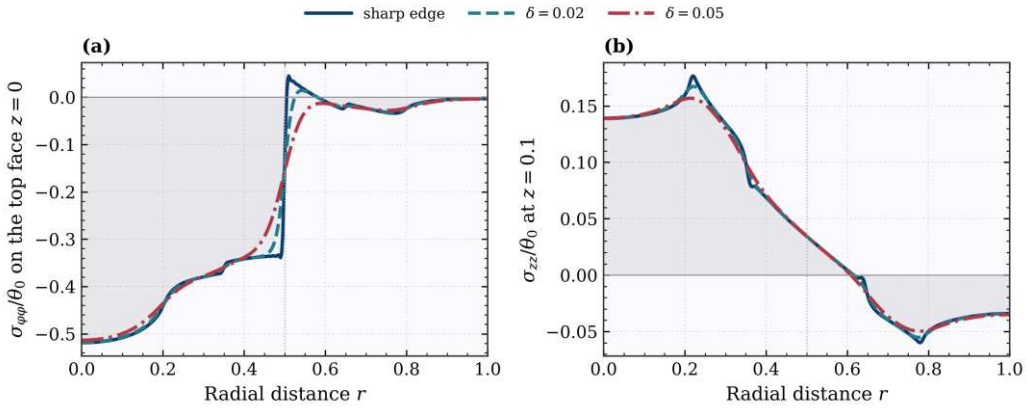


Fig. 3 Effect of smoothing the edge of the heated disk at $t = 0.3$ ($N_m = 160$): (a) hoop stress on the top face; (b) axial stress at $z = 0.1$

Table 5 Edge-sensitivity test at $t = 0.3$: hoop stress on the axis of the top face, change of the hoop stress across the edge ($r = 0.45 \to 0.55$) and minimum axial stress at $z = 0.1$

Edge	N_m	$\sigma_{\varphi\varphi}/\theta_0$ at $r = 0$	Change across edge	Min. σ_{zz}/θ_0 at $z = 0.1$
sharp	40	-0.5190	0.3568	-0.0558
sharp	80	-0.5190	0.3531	-0.0583
sharp	160	-0.5190	0.3526	-0.0599
sharp	320	-0.5190	0.3525	-0.0609
$\delta = 0.02$	40	-0.5179	0.3423	-0.0539
$\delta = 0.02$	80	-0.5181	0.3465	-0.0549
$\delta = 0.02$	160	-0.5182	0.3474	-0.0552
$\delta = 0.02$	320	-0.5182	0.3476	-0.0553
$\delta = 0.05$	40	-0.5132	0.2548	-0.0494
$\delta = 0.05$	80	-0.5135	0.2617	-0.0497
$\delta = 0.05$	160	-0.5136	0.2635	-0.0498
$\delta = 0.05$	320	-0.5136	0.2639	-0.0498

9 Application with AISI 4340 alloy-steel constants

9.1 Material data and status of the parameters

AISI 4340 is a medium-carbon Ni–Cr–Mo low-alloy steel with high strength, toughness and hardenability. Its chemical composition according to SAE J404 (SAE 2009) is given in Table 6. Table 7 separates three kinds of quantities: room-temperature handbook properties (MakeItFrom.com 2026), constants derived from them, and model parameters. The handbook values are typical room-temperature values; the elastic, thermal and thermophysical constants used here vary only weakly with the heat-treatment condition, whereas the strength values (not used in the linear analysis) depend strongly on it. The relaxation parameters A, a and b_v and the heat-law parameters τ_v, ω, β and the kernel have not been measured for AISI 4340; they are illustrative values, and the resulting fields are model predictions rather than validated material-specific responses. The linear theory assumes $|\theta/T_0| \ll 1$ and temperature-independent properties; for large temperature rises the temperature dependence of the steel properties would have to be included.

Table 6 Chemical composition of AISI 4340 alloy steel (wt.%; SAE 2009)

	C	Mn	Si	Ni	Cr	Mo
wt.%	0.38–0.43	0.60–0.80	0.15–0.35	1.65–2.00	0.70–0.90	0.20–0.30

P ≤ 0.035, S ≤ 0.040, Fe balance.

Table 7 Quantities used in the computations: (a) room-temperature handbook properties of AISI 4340 (MakeItFrom.com 2026); (b) derived constants; (c) assumed model parameters (illustrative, not measured for AISI 4340)

Quantity	Value
(a) Density ρ	7850 kg/m^3
(a) Young's modulus E	190 GPa
(a) Poisson's ratio ν	0.29
(a) Thermal conductivity k	44 W/(m K)
(a) Specific heat C_E	470 J/(kg K)
(a) Thermal expansion α_T	13 × 10^{-6} K^{-1}
(a) Reference temperature T_0	293 K
(b) Lamé constants λ, μ	101.7 GPa, 73.6 GPa
(b) $\lambda + 2\mu$; bulk modulus K	249.0 GPa; 150.8 GPa
(b) $\gamma = (3\lambda + 2\mu)\alpha_T$	5.88 × 10^6 N/(m^2 K)
(b) c_0; η_0	5632 m/s; 8.385 × 10^4 s/m^2
(b) ε; $\widehat{\mu}$; κ	0.0110; 0.2958; 0.6056
(b) Unit of length $1/(c_0\eta_0)$	2.12 nm
(b) Unit of time $1/(c_0^2\eta_0)$	0.376 ps
(b) Stress unit $\gamma\Delta T_0$ ($\Delta T_0 = 5$ K)	29.4 MPa
(c) Relaxation constants A, a, b_v	0–0.3, 0.5, 0.5
(c) Heat law τ_v, ω	0.25, 0.2 (0.094 ps, 0.075 ps)
(c) Fractional order β; kernel	0.25–0.70; see Table 2

9.2 Physical scales of the nondimensional results

The nondimensionalization (18) implies a unit of length $1/(c_0\eta_0) = 2.12$ nm and a unit of time $1/(c_0^2\eta_0) = 0.376$ ps for AISI 4340. The reference geometry $R_0 = h = 1$, $b = 0.5$ thus corresponds to a cylinder of 2.12 nm, the evaluation time $t = 0.3$ to 0.113 ps, and $\tau_v = 0.25$ and $\omega = 0.2$ to 0.094 ps and 0.075 ps. At these scales the continuum description itself is at the limit of its validity. For a macroscopic component, for example $R_0 = h = 10$ mm, the elastic transit time h/c_0 is 1.78 μs and the thermal diffusion time $h^2\eta_0$ is 8.4 s, so that at the macroscopic scale the illustrative memory and relaxation times are much shorter than the elastic transit time. However, this scale separation alone does not establish that the fractional Green–Naghdi heat law reduces to the classical Biot theory; such a reduction requires an appropriate constitutive limit or a separate asymptotic analysis. Therefore, the present results, computed with the coupling constants κ, $\widehat{\mu}$ and ε of AISI 4340, are interpreted as a nondimensional parametric investigation rather than validated predictions for macroscopic steel components. Dimensional counterparts of the computations, at a structural and at a sub-micron scale, are given in Section 9.10.

Because the governing equations are linear, the computed fields are normalized by the prescribed surface temperature rise. For an illustrative applied temperature increment of $\Delta T_0 = 5$ K, the corresponding stress scale is $\gamma\Delta T_0 = 29.4$ MPa; for example, a normalized axial stress $\sigma_{zz}/\theta_0 = -1$ corresponds to -29.4 MPa. This temperature increment is consistent with the small-temperature-perturbation assumption of the linear formulation.

Unless otherwise stated, the computations use $R_0 = 1$, $h = 1$, $b = 0.5$, $\beta = 0.5$, $\tau_v = 0.25$, $\omega = 0.2$, the quadratic kernel, $A = 0.1$, $a = 0.5$ and $b_v = 0.5$, and the fields are evaluated at $t = 0.3$. Axial distributions are shown along the axis $r = 0$; the shear stress, which vanishes on the axis, is shown at $r = b$.

9.3 Comparison of heat transport laws

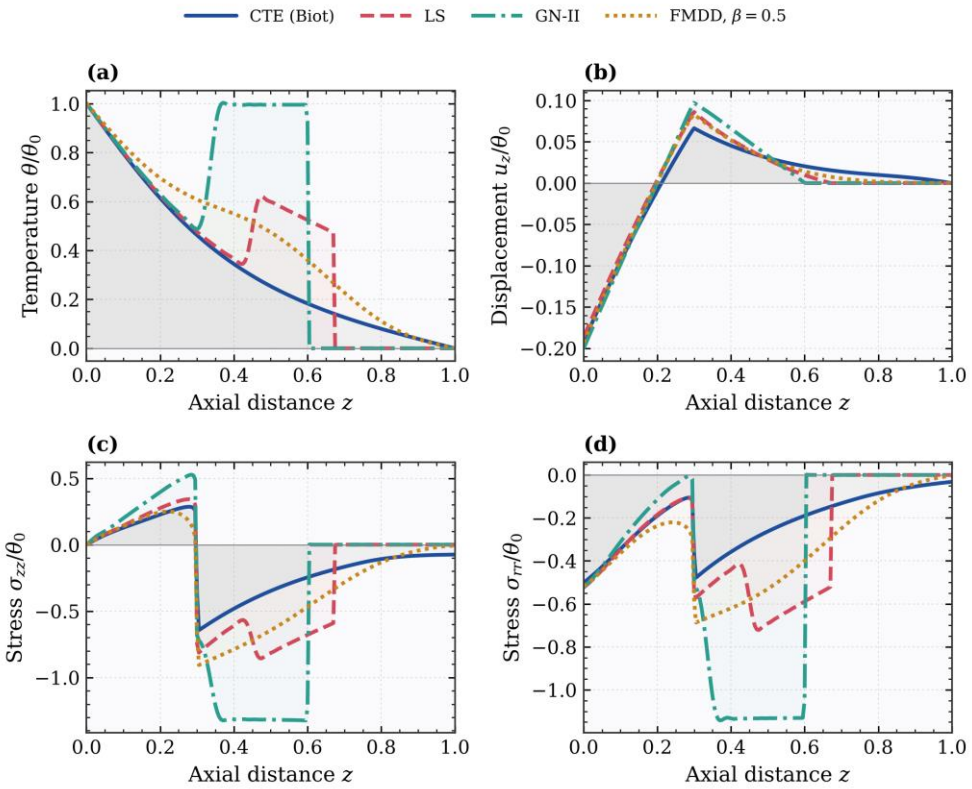


Fig. 4 Axial distributions on the axis at $t = 0.3$ for the Biot (CTE), Lord–Shulman (LS), Green–Naghdi II (GN-II) and FMDD laws: (a) temperature, (b) axial displacement, (c) axial stress, (d) radial stress

Fig. 4 compares the four heat transport laws along the axis. With the Biot law the temperature decreases monotonically and is non-zero over the whole height. The Lord–Shulman and Green–Naghdi II laws produce sharp thermal fronts at $z \approx 0.67$ and $z \approx 0.60$, ahead of which the medium is undisturbed. The FMDD law lies between these limits: at $z = 0.2$ its temperature, 0.70, is the highest of the four (0.61–0.63 for the others), and its profile decays smoothly without a jump.

The axial displacement is much less sensitive to the heat law: the surface value $u_z(0)/\theta_0$ ranges from -0.186 to -0.200, and all curves change slope at the elastic front $z = t = 0.3$. The stresses are more sensitive. In this nondimensional reference case the minimum axial stress is -0.64 for Biot, -0.86 for Lord–Shulman, -0.91 for FMDD and -1.32 for Green–Naghdi II (per unit θ_0; multiply by $\gamma\Delta T_0$ for a dimensional value). The radial stress follows the same ranking, with minima between -0.50 and -1.14.

9.4 Effect of the fractional order

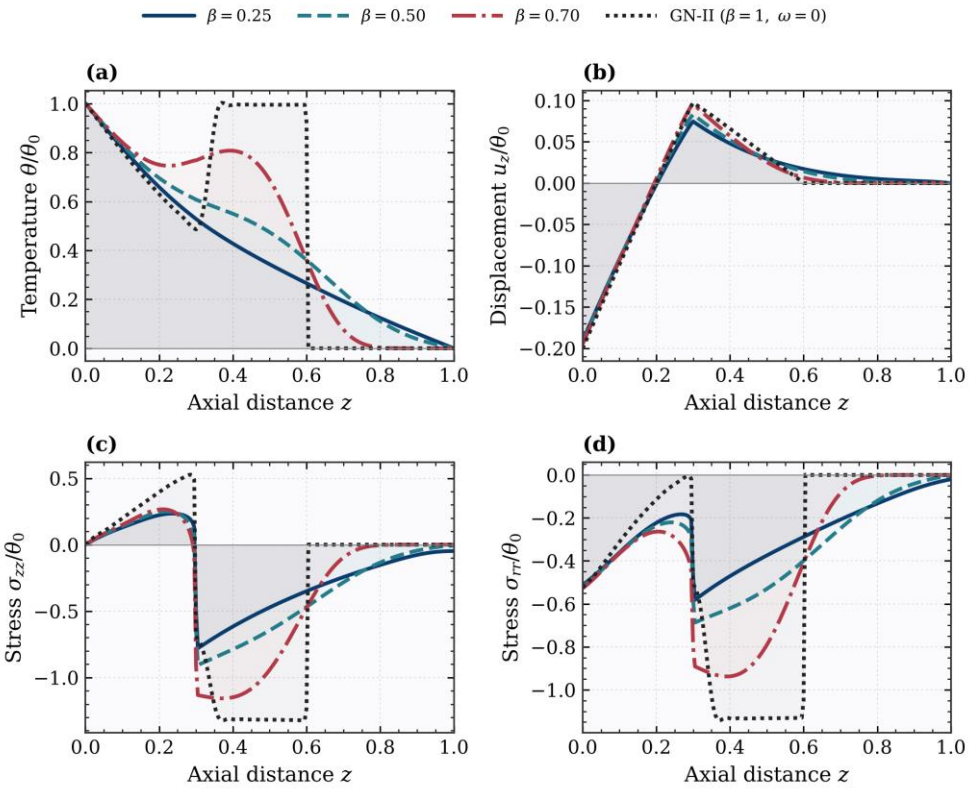


Fig. 5 Effect of the fractional order on the axial distributions at $t = 0.3$ (quadratic kernel, $\omega = 0.2$); the Green–Naghdi II limit ($\beta = 1$, $\omega = 0$) is shown for reference

For admissible fractional orders (Table 2), increasing β from 0.25 to 0.70 changes the thermal response from diffusion-like towards wave-like (Fig. 5). On the axis at $z = 0.2$ the temperature rises from 0.66 to 0.70 and 0.75, while the disturbed region contracts; for $\beta = 0.70$ a steep front develops that approaches the Green–Naghdi II front. The minimum axial stress changes from -0.78 to -0.91 and -1.16, and the minimum radial stress from -0.58 to -0.94. The displacement is only weakly affected. Within the nondimensional model, a larger fractional order therefore concentrates the thermal disturbance and increases the compressive stresses behind the elastic front.

9.5 Effect of the memory kernel

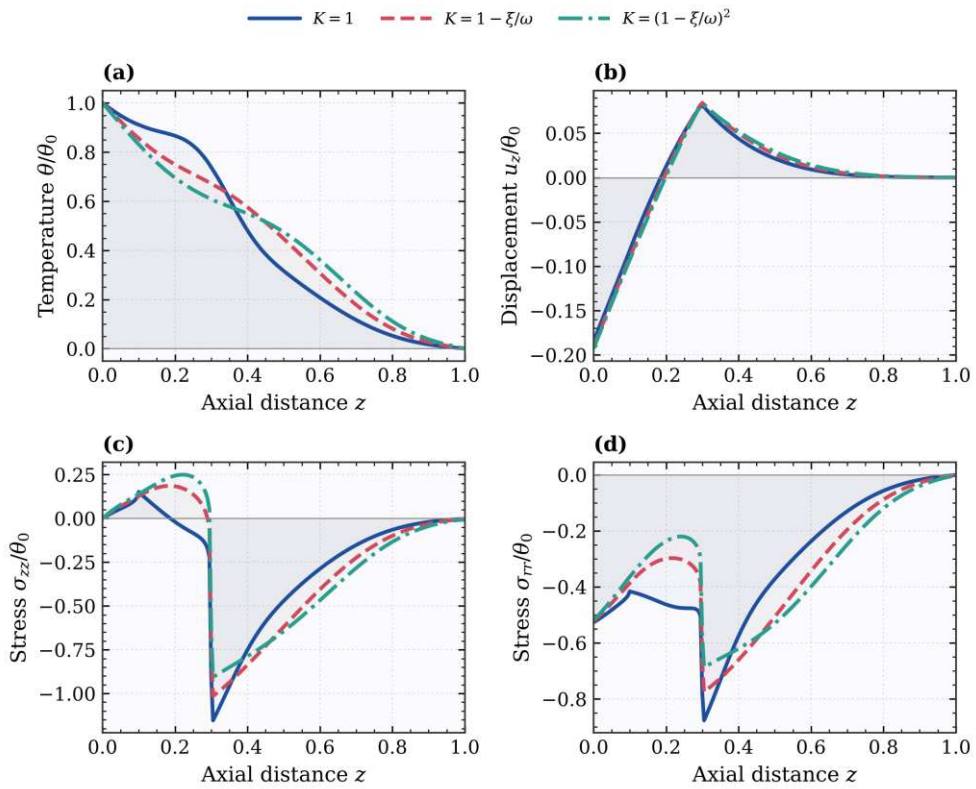


Fig. 6 Effect of the kernel of the memory-dependent derivative on the axial distributions at $t = 0.3$ ($\beta = 0.5$, $\omega = 0.2$)

Fig. 6 shows the influence of the kernel, which weights the past heat flux over $[t - \omega, t]$. The constant kernel gives the same weight to the whole window and the strongest memory: the near-surface temperature remains high ($\theta/\theta_0 = 0.87$ at $z = 0.2$) and a secondary disturbance appears near $z \approx 0.2$, associated with the abrupt end of the memory window. The linear and quadratic kernels weight older history less; their profiles are smoother and the near-surface temperature is lower (0.75 and 0.70). The minimum axial stress changes from -1.15 ($K = 1$) to -1.02 (linear) and -0.91 (quadratic). The kernel is thus an additional modelling degree of freedom, which would have to be identified from measurements for a specific material.

9.6 Effect of viscoelastic relaxation

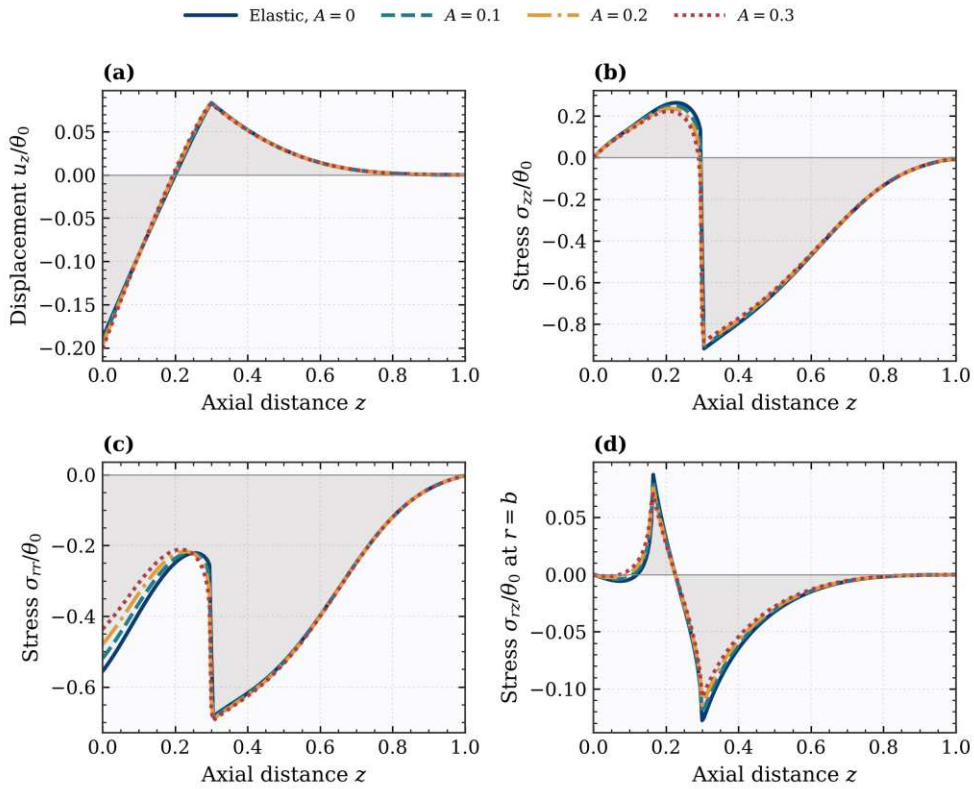


Fig. 7 Effect of the relaxation constant A at $t = 0.3$: (a) axial displacement, (b) axial stress and (c) radial stress on the axis; (d) shear stress at $r = b$

The relaxation constant A controls how strongly the shear modulus relaxes (Fig. 7). The temperature is practically independent of A because the thermoelastic coupling of AISI 4340 is weak ($\varepsilon = 0.011$). As A increases from 0 to 0.3, the effective shear stiffness decreases, the surface displacement changes from -0.189 to -0.201 and the minimum axial stress from -0.918 to -0.883. The effect is strongest near the heated face, where the radial stress on the axis changes from -0.556 (elastic) to -0.437 ($A = 0.3$). Since A, a and b_v are illustrative, these trends indicate the sensitivity of the model to hereditary relaxation rather than quantified properties of the steel.

9.7 Radial distributions

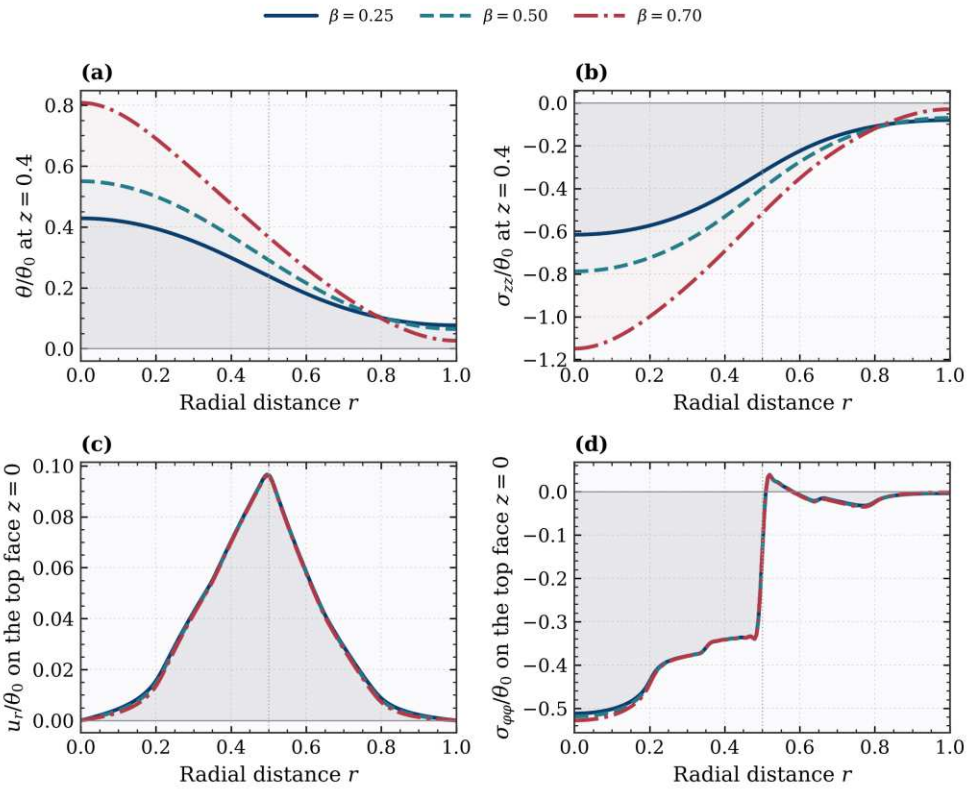


Fig. 8 Radial distributions at $t = 0.3$ for three admissible fractional orders: (a) temperature and (b) axial stress at $z = 0.4$; (c) radial displacement and (d) hoop stress on the top face. The dotted line marks the edge of the heated disk $r = b$

Radial distributions are shown in Fig. 8. At $z = 0.4$ the temperature is highest on the axis and decreases towards the insulated lateral face; a larger β sharpens this profile, from 0.43 on the axis and 0.08 at $r = R_0$ for $\beta = 0.25$ to 0.81 and 0.03 for $\beta = 0.70$. The axial stress at the same depth follows the temperature (-0.62 to -1.15 on the axis). On the top face the radial displacement reaches its maximum, about 0.096, at $r \approx b$, where the expanding heated core pushes outward against the unheated annulus. The hoop stress is compressive, about -0.52, inside the heated disk and changes sharply across $r = b$; as shown in Section 8.4, the size of this change depends on the idealization of the heated edge. These surface quantities are nearly independent of β, because they are governed by the prescribed surface temperature.

9.8 Three-dimensional distributions

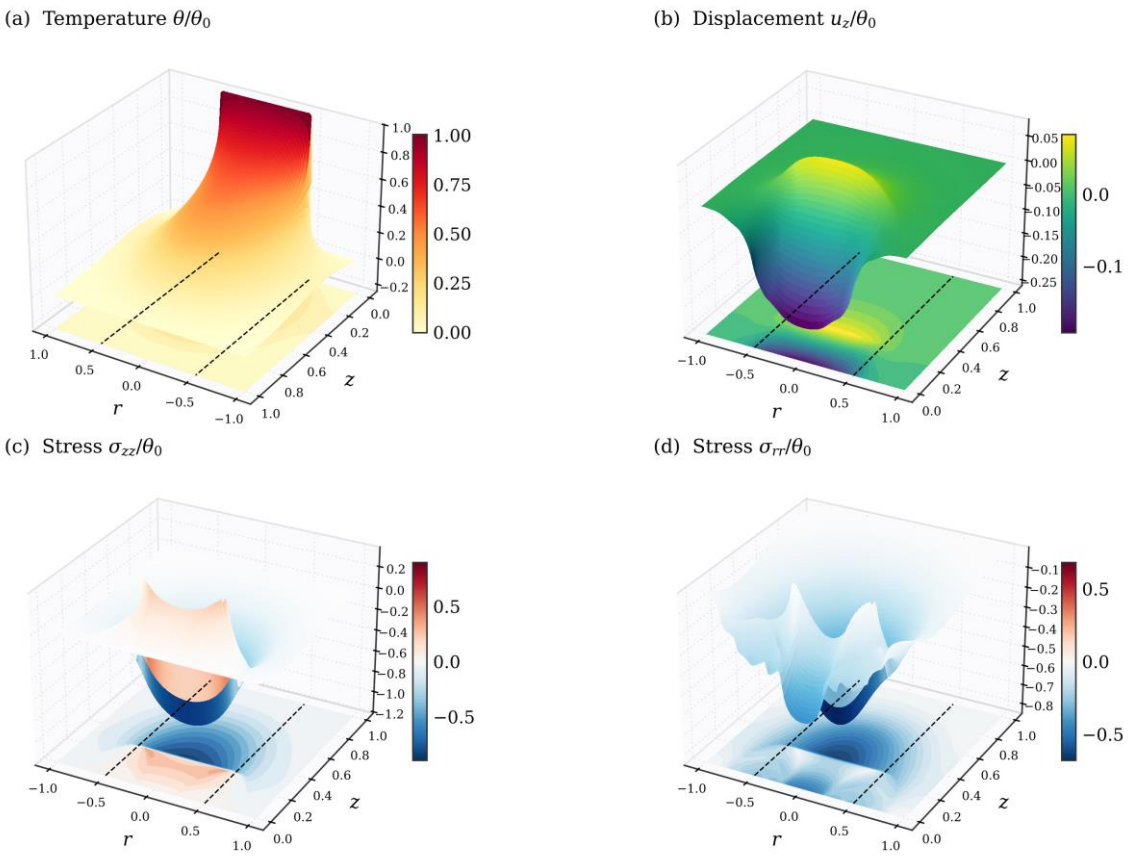


Fig. 9 Distributions over the meridian plane at $t = 0.3$ (FMDD, $\beta = 0.5$), mirrored about the axis, with contour maps projected on the base; dashed lines mark $r = \pm b$. (a) Temperature, (b) axial displacement, (c) axial stress, (d) radial stress

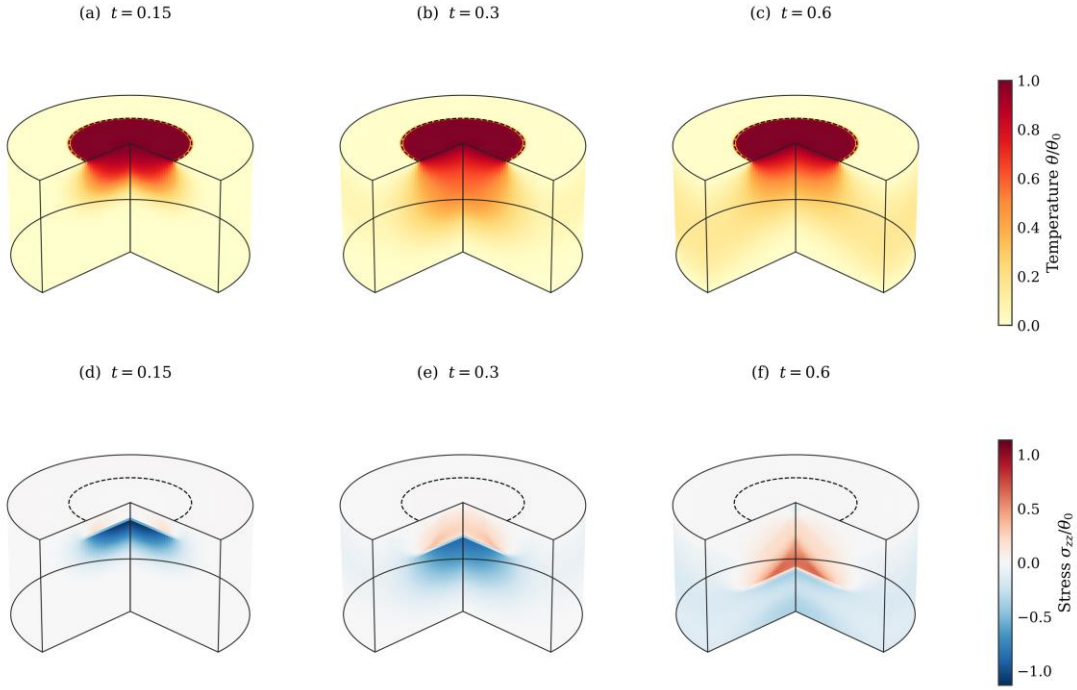


Fig. 10 Cut-away views of the cylinder showing the temperature (a)–(c) and the axial stress (d)–(f) at $t = 0.15$, 0.3 and 0.6 (FMDD, $\beta = 0.5$). Each row uses one colour scale; the dashed circle marks the edge of the heated disk

Figs. 9 and 10 present the fields over the whole cylinder. The temperature surface shows the plateau under the heated disk and its decay into the interior. The axial displacement forms a bowl under the heated disk with a ridge at the elastic front, and the axial and radial stresses show a compressive region behind the elastic front, $z \approx 0.3$, with tensile regions near the free face. The cut-away views follow these fields in time on common colour scales: the heated zone

grows from a thin layer under the disk at $t = 0.15$ to a region that occupies most of the upper half at $t = 0.6$, while the compressive axial-stress front (minimum -1.13 at $t = 0.15$) travels downward and leaves a tensile zone behind it (maximum 0.63 at $t = 0.6$).

9.9 Time evolution and the role of the finite height

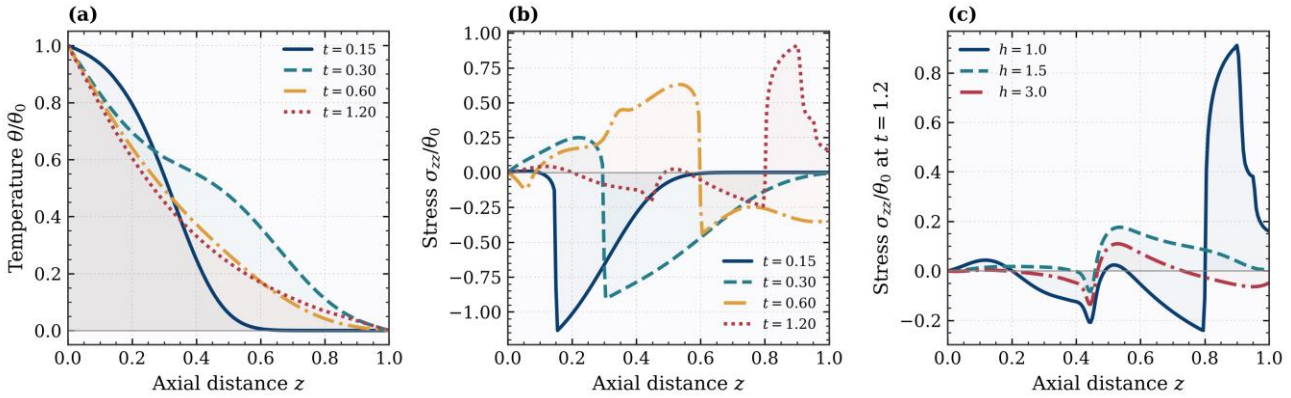


Fig. 11 (a) Temperature and (b) axial stress on the axis at four instants; (c) axial stress at $t = 1.2$ for three heights h. Nondimensional times; $t = 1$ corresponds to 0.376 ps for the AISI 4340 constants

Fig. 11 summarizes the time evolution on the axis. The temperature at mid-height first rises to 0.47 at $t = 0.3$ and then settles near 0.24, approaching the steady profile imposed by the boundary temperatures. The minimum axial stress weakens with time (-1.13, -0.91, -0.44 and -0.24 at $t = 0.15$, 0.3, 0.6 and 1.2), while the tensile stress grows. At $t = 1.2$ the elastic front has been reflected by the clamped base, and the reflected wave produces a tensile peak of 0.91 near $z = 0.9$. Fig. 11(c) isolates this finite-height effect: for $h = 1.5$ and $h = 3$, where the front has not yet reached the base, the maximum tensile stress is only 0.18 and 0.11. Under the assumed constraints, the model therefore predicts that the base region of a short cylinder can become the most strongly loaded region after the reflection; this prediction has not been compared with measurements.

9.10 Dimensional case studies

To relate the formulation to physical quantities, two cases were computed with the AISI 4340 constants of Table 7 in SI units, both for an applied temperature rise $\Delta T_0 = 5$ K (stress unit $\gamma \Delta T_0 = 29.4$ MPa). The same solver was used; only the geometric and time parameters were converted with Eq. (18).

Case I: structural-scale cylinder. A cylinder with $R_0 = h = 20$ mm is heated over its whole top face ($b = R_0$) with the classical (Biot) law and $A = 0$. For this scale the elastic transit time h/c_0 is 3.55 μs and the thermal diffusion time $h^2 \rho C_E / k$ is 33.5 s, so the response is quasi-static, the axial stress vanishes and the radial stress follows the uniaxial-strain relation $\sigma_{rr} = -2\mu\gamma\theta/(\lambda + 2\mu)$. In this limit the temperature has the exact series solution of the diffusion equation with diffusivity $k/[\rho C_E(1 + \varepsilon)]$, which provides an independent benchmark in physical units. Fig. 12(a), (b) and Table 8 show that the state-space solution reproduces the exact temperature to within 2×10^{-4} K and the radial stress to within 7×10^{-4} MPa at $t = 1$, 10 and 100 s; the computed axial stress is below 3×10^{-12} MPa, i.e. zero to round-off. The surface radial stress reaches -17.4 MPa in the steady state, $-2\hat{\mu}\gamma\Delta T_0$ exactly. The agreement between the state-space solution and the exact quasi-static solution validates the numerical implementation in the classical Biot limit. It does not constitute experimental validation of the fractional memory-dependent heat transport law; comparisons with measurements are given in Section 10.

Fig. 12(c) applies the FMDD law at the same scale, with the illustrative parameters of Table 7 converted to seconds. The temperature at mid-height reaches 90% of its steady value after about 10 s with the Biot law but after about 1.5×10^{-2} s ($\beta = 0.25$) and 2×10^{-4} s ($\beta = 0.5$) with the FMDD law, and with an overshoot. The steady state is the same for all laws. This is a property of the heat law and not of the solution method: Eq. (8) contains no Fourier term, and its transform $\Lambda(s) \simeq \tau_v^\beta s^{\beta+1}$ at small s produces a time scale of order $(h^2 \tau_v^\beta)^{1/(1+\beta)}$ instead of the diffusion time $h^2 \eta_0$. At the structural scale, the FMDD model with the illustrative sub-picosecond parameters therefore produces thermal transients substantially faster than those predicted by classical Fourier conduction. This discrepancy indicates that the adopted fractional and memory parameters cannot be transferred directly between physical scales without calibration. Consequently, the structural-scale FMDD results are interpreted as a constitutive sensitivity test rather than quantitative predictions for AISI 4340 steel. A physically calibrated extension may require an additional Fourier contribution, as in Green–Naghdi type III formulations; such an extension would require a separate derivation and numerical investigation.

Case II: sub-micron cylinder subjected to step-temperature excitation and examined at picosecond time scales. A cylinder with $R_0 = h = 0.5$ μm is heated over a disk of radius $b = 0.25$ μm (edge width $\delta = 10$ nm) with $A = 0.1$. At this scale the time scales of the heat laws become comparable with the elastic transit time. Picosecond ultrasonics provides an experimental framework for investigating ultrafast stress generation and acoustic wave propagation in solids (Thomsen et al. 1986). Time-resolved optical measurements can detect changes in reflectivity associated with transient strain and acoustic waves; the predicted surface displacement may therefore be related to experimentally accessible optical signals through an appropriate measurement model. Fig. 13 compares the Biot, Lord–Shulman and FMDD laws. At $t = 50$ ps the temperature rise exceeds 0.5 K down to a depth of 55 nm with the Biot and Lord–Shulman laws and down to 212 nm with the FMDD law (Fig. 13(a)). At $t = 100$ ps the axial stress on the axis ranges from -1.43 to 1.75 MPa with the Biot law and from -13.8 to 3.38 MPa with the FMDD law (Fig. 13(b)). The Biot and Lord–Shulman results nearly coincide, because the Lord–Shulman relaxation time of 0.075 ps is negligible at this time scale. The surface displacement (Fig. 13(c)) is -7.3 pm (Biot) and -20.3 pm (FMDD) at $t = 150$ ps. Its slope changes when the stress wave reflected by the clamped base returns to the heated face: comparison with a cylinder three times taller shows the first deviation at 181.5 ps (Biot) and 179.5 ps (FMDD), against the elastic two-way transit time $2h/c_0 = 177.6$ ps. Doubling N_m or N changes the Case II values by less than 0.4%.

The sub-micron results must be interpreted within the limitations of the adopted continuum thermoviscoelastic formulation. The room-temperature elastic and thermal constants of AISI 4340 are used as representative material parameters, and the fractional order, memory interval and viscoelastic relaxation parameters have not been calibrated experimentally for this steel. Furthermore, under ultrafast laser excitation, electron–phonon nonequilibrium may influence energy transport before thermal equilibrium is established (Singh 2025); such effects are not represented explicitly in the present single-temperature formulation. Accordingly, the differences between the Biot, Lord–Shulman and FMDD predictions should be regarded as model-dependent theoretical predictions; they do not demonstrate the experimental superiority of any heat transport law. Future pump–probe measurements could provide the data required to identify the memory parameters and assess the physical validity of the formulation.

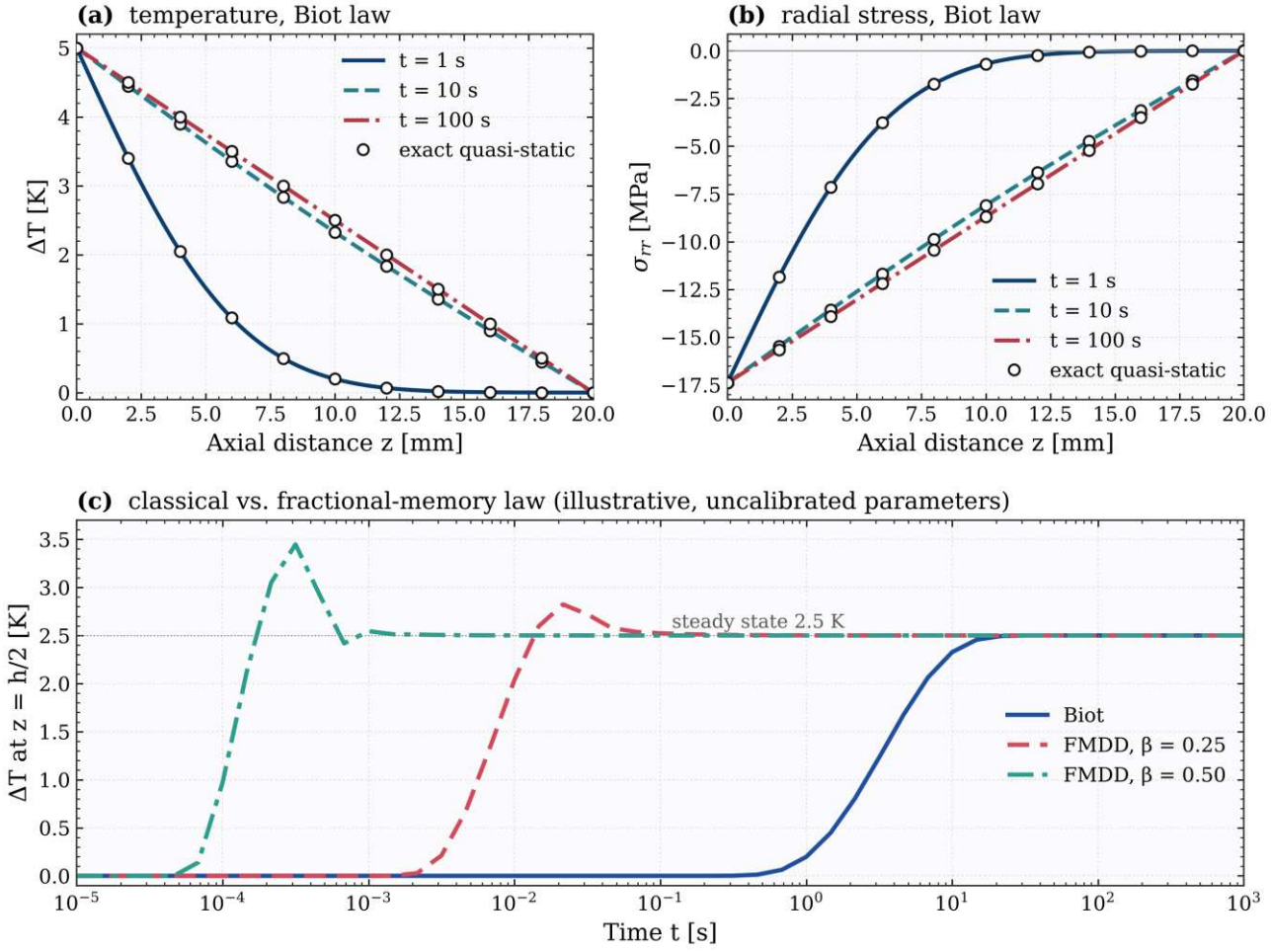


Fig. 12 Structural-scale AISI 4340 cylinder ($R_0 = h = 20$ mm, $\Delta T_0 = 5$ K). (a) Temperature distribution and (b) radial stress predicted by the classical Biot model (lines) and compared with the exact quasi-static solution (markers) at $t = 1$, 10 and 100 s. (c) Comparison of classical and fractional memory-dependent thermal responses at mid-height using illustrative, uncalibrated memory parameters

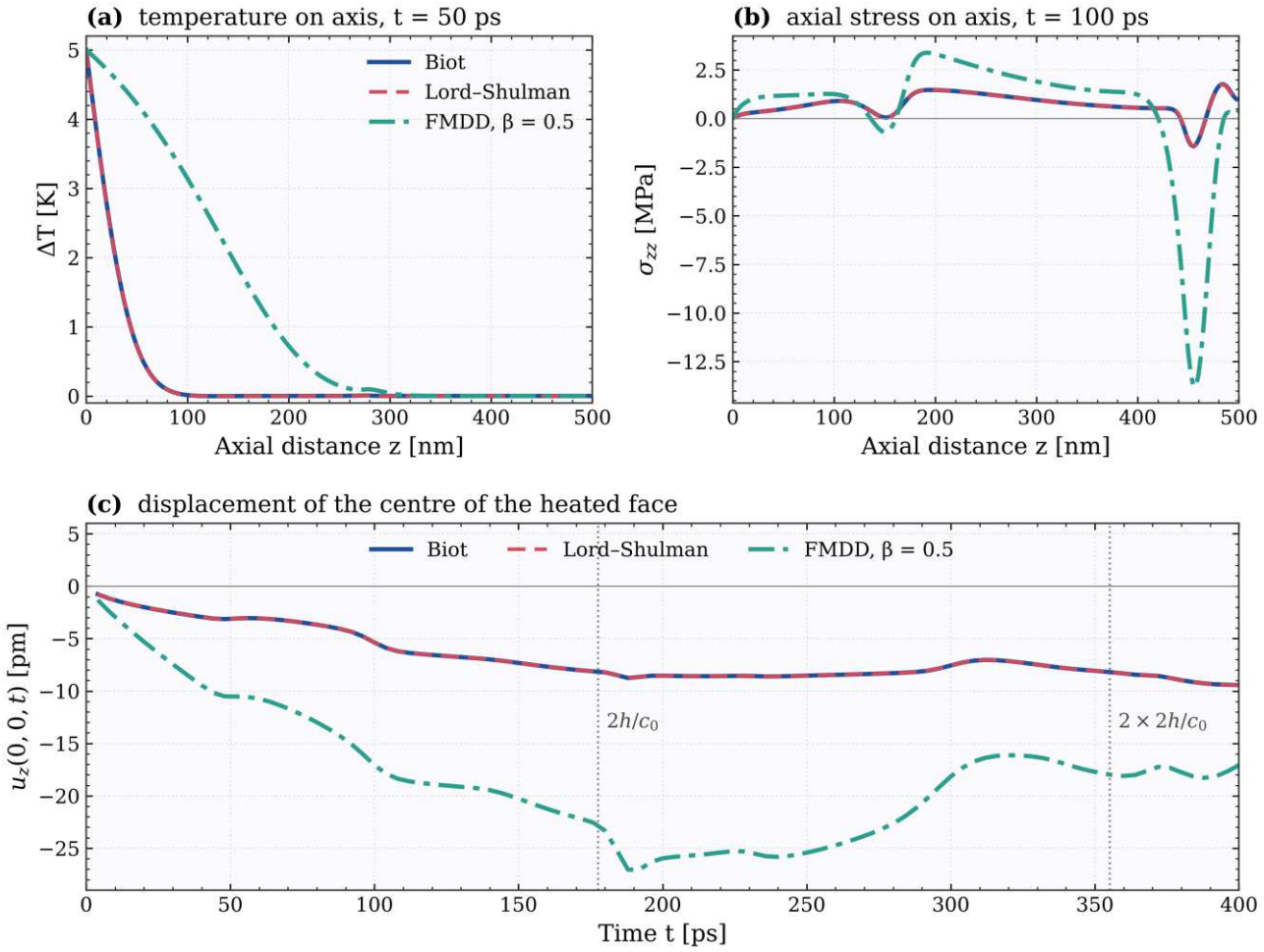


Fig. 13 Predicted transient response of an AISI 4340 cylinder with $R_0 = h = 0.5$ μm under localized step-temperature excitation at picosecond time scales ($b = 0.25$ μm, $\Delta T_0 = 5$ K, $A = 0.1$). (a) Axial temperature distribution at $t = 50$ ps. (b) Axial stress distribution at $t = 100$ ps. (c) Surface displacement history at the centre of the heated face; dotted lines mark multiples of $2h/c_0$. The results compare the Biot, Lord–Shulman and FMDD heat transport laws. The fractional-memory parameters are illustrative and have not been experimentally calibrated for AISI 4340

Table 8 Case I ($R_0 = h = 20$ mm, $\Delta T_0 = 5$ K, Biot law): state-space (SS) solution and exact quasi-static solution (exact) of the temperature rise and the radial stress

t [s]	z [mm]	ΔT SS [K]	ΔT exact [K]	σ_{rr} SS [MPa]	σ_{rr} exact [MPa]
1	5	1.5165	1.5164	-5.276	-5.275
1	10	0.1976	0.1975	-0.687	-0.687
1	15	0.0101	0.0101	-0.035	-0.035
10	5	3.6276	3.6274	-12.620	-12.619
10	10	2.3268	2.3267	-8.095	-8.094
10	15	1.1275	1.1275	-3.922	-3.922
100	5	3.7502	3.7500	-13.046	-13.046
100	10	2.5001	2.5000	-8.698	-8.697
100	15	1.2501	1.2500	-4.349	-4.349

10 Experimental benchmarking and physical limitations of the fractional-memory steel model

Sections 8 and 9 verified the solution numerically and explored the model parametrically. This section compares the model with published measurements on AISI 4340 and identifies what the comparisons can and cannot establish. Three kinds of results are distinguished in what follows: *experimental benchmarking*, in which a model prediction is compared with a measurement; *numerical verification*, in which the solution is compared with an independent solution of the same equations; and *theoretical predictions*, which have not been compared with measurements.

10.1 Experimental studies on AISI 4340 steel

Published experiments on AISI 4340 were screened against the assumptions of the present model: linear thermoviscoelasticity with temperature-independent properties, a small temperature rise ($|\theta/T_0| \ll 1$), no phase transformation, and boundary conditions that can be represented by the model. Table 9 lists the studies retained and the

use made of each. The tensile-bar measurements of Burns et al. (2025) involve temperature changes below 1 K in the elastic range and satisfy all of these assumptions; the ultrasonic wave speed is a small-amplitude elastic property. The laser-hardening experiments of Fakir et al. (2018) on 4340 cylinders do not satisfy them (Section 10.3) and are used for discussion only.

Table 9 Published experiments on AISI 4340 steel and their compatibility with the present model

Study	Measured quantity	Conditions	Compatible with the model	Use
Burns et al. (2025)	Temperature–stress slope (infrared camera)	Tensile bars, 80 mm gauge, elastic loading at 256 MPa/s and fast elastic unloading; $\lvert\theta\rvert < 1$ K	Yes	Quantitative benchmark (Sections 10.2, 10.4)
Evident Scientific (2026)	Longitudinal ultrasonic velocity	Small-amplitude elastic waves	Yes	Quantitative benchmark (Section 10.2)
Fakir et al. (2018)	Surface temperature (pyrometer), hardness profile	15 mm cylinder rotating at 5000 rpm, 2–3 kW laser for 1.5 s; peak 1400–1500 K, austenitization and surface melting	No	Discussion only (Section 10.3)

10.2 Comparison with published thermoelastic and acoustic measurements

Isentropic thermoelastic effect. Burns et al. (2025) measured with a high-speed infrared camera the temperature of normalized AISI 4340 tensile bars (gauge length 80 mm) loaded elastically at 256 MPa/s for about 2 s, and the heating caused by the fast elastic unloading at fracture (strain rate above 10^3 s^{-1}). They reported a temperature–stress slope of -0.65 ± 0.05 K/GPa during loading and -1.2 ± 0.3 K/GPa on unloading. For a bar under the uniform uniaxial stress $\sigma(t)$ the dilatation is $e = (1-2\nu)\sigma/E + 3\alpha_T\theta$, and the dimensional form of the heat law (8) becomes, in the Laplace domain,

$$k\,\frac{d^2\bar\theta}{dx^2} = \Lambda_d(s)[\rho C_\sigma \bar\theta + \alpha_T T_0\,\bar\sigma], \qquad \rho C_\sigma = \rho C_E + 3\alpha_T\gamma T_0, \tag{53}$$

where $\Lambda_d(s)$ is the dimensional symbol of the heat law: $\Lambda_d = s$ for the Biot law and $\Lambda_d(s) = \Lambda(st_u)/t_u$ for the FMDD law, with Λ from Eq. (28) and $t_u = 1/(c_0^2\eta_0)$. If the temperature is uniform, the left-hand side vanishes; since Λ_d acts on functions that vanish for $t<0$, $\rho C_\sigma\theta + \alpha_T T_0\sigma = 0$ for every heat law, which is Kelvin's isentropic relation

$$\frac{\theta}{\sigma} = -\frac{\alpha_T T_0}{\rho C_\sigma} = -1.014 \text{ K/GPa}. \tag{54}$$

To include heat exchange with the grips, the ends $x = \pm\ell$ of the gauge length ($\ell = 40$ mm) are held at the reservoir temperature. The solution of Eq. (53), averaged over the extensometer length $\lvert x\rvert \le a$ ($a = 25$ mm), is

$$\bar\theta_m = -\frac{\alpha_T T_0\,\bar\sigma}{\rho C_\sigma}\Big[1 - \frac{\sinh(qa)}{qa\cosh(q\ell)}\Big], \qquad q = \Big[\frac{\rho C_\sigma \Lambda_d(s)}{k}\Big]^{1/2}, \quad \bar\sigma = \frac{\dot\sigma}{s^2}, \tag{55}$$

and is inverted with Eq. (52). For the Biot law the inversion agrees with the exact eigenfunction series of the same problem to within 7×10^{-5} K.

With the Biot law the predicted slope during loading is -1.014 K/GPa (Fig. 14(a)). It differs from the isentropic value (54) by less than 0.1%, because the conduction time over the gauge length, $\ell^2\rho C_\sigma/k = 137$ s, is much longer than the 2 s loading. Table 10 gives the errors. The measured unloading slope, -1.2 ± 0.3 K/GPa, agrees with Eq. (54) within the experimental uncertainty (absolute error 0.19 K/GPa, relative error 15%). The measured loading slope is 64% of the predicted value (absolute error 0.36 K/GPa); this deficit is discussed in Section 10.5. Because Burns et al. (2025) reported slopes rather than tabulated temperature histories, the root-mean-square errors in Table 10 are those of the temperature over the elastic range 0–0.51 GPa computed from the reported mean slopes. The thermoelastic coupling of the present formulation for AISI 4340, $\varepsilon = 0.011$ in nondimensional form, is consistent with the unloading measurement, which is the closest to isentropic conditions.

Longitudinal wave speed. The wave speed of the model, $c_0 = [(\lambda+2\mu)/\rho]^{1/2} = 5632$ m/s with the handbook constants of Table 7, is 3.7% lower than the measured ultrasonic longitudinal velocity of 4340 steel, 5850 m/s (Evident

Scientific 2026). The computed fronts and base reflections are therefore delayed by about 4%: the two-way transit time of Case II is 177.6 ps against 170.9 ps with the measured velocity, and the transit time of Case I is 3.55 µs against 3.42 µs (Fig. 14(c)). The measured velocity corresponds to $E = 205$ GPa for $\nu = 0.29$. Because κ and $\hat{\mu}$ depend only on ν, this modulus would change the nondimensional results only through ε, which would increase from 0.0110 to 0.0119; the physical length and time scales would change in proportion to $1/c_0$.

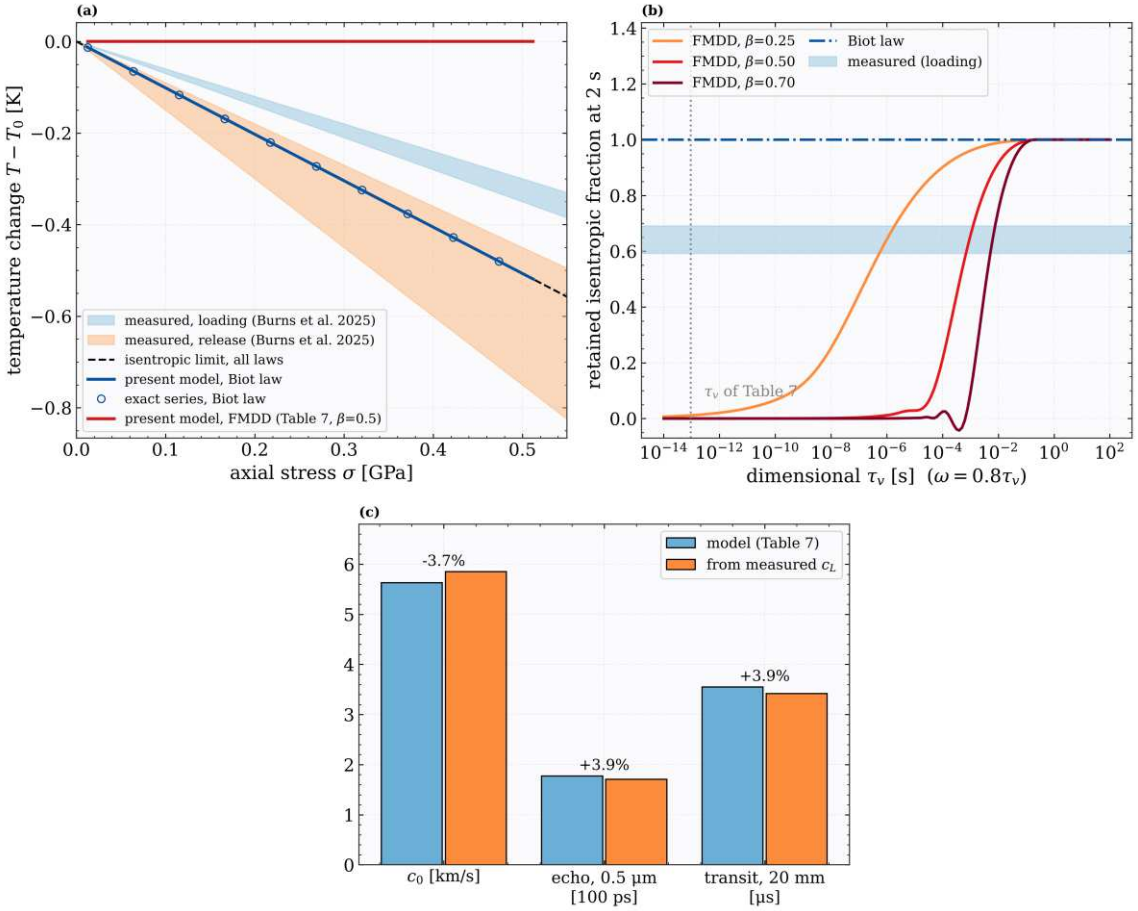


Fig. 14 Comparison with measurements on AISI 4340 steel. (a) Temperature change against axial stress in a tensile bar loaded at 256 MPa/s: measured slopes during loading and unloading (Burns et al. 2025, bands show the reported uncertainties), the isentropic relation (54), and the predictions of Eq. (55) with the Biot law (line; markers: exact series) and with the FMDD law using the illustrative parameters of Table 7. (b) Fraction of the isentropic temperature change retained after 2 s against the dimensional memory time τ_v ($\omega = 0.8\tau_v$, quadratic kernel); the band shows the measured fraction. (c) Longitudinal wave speed, two-way transit time of the 0.5 µm cylinder and transit time of the 20 mm cylinder from the constants of Table 7 and from the measured ultrasonic velocity (Evident Scientific 2026)

Table 10 Experimental benchmarking: model predictions, measured values and errors (AISI 4340)

Quantity	Measured	Model	Absolute error	Relative error	RMSE
Thermoelastic slope, fast unloading [K/GPa]	-1.2 ± 0.3	-1.014 (all heat laws)	0.19	15%	0.055 K
Thermoelastic slope, loading at 256 MPa/s [K/GPa]	-0.65 ± 0.05	-1.014 (Biot)	0.36	56%	0.11 K
Same, FMDD with the illustrative parameters of Table 7	-0.65 ± 0.05	≈ 0	0.65	100%	0.19 K
Isentropic slope with the constants used by Burns et al. [K/GPa]	—	-0.963	—	5.3% (vs. Table 7)	—
Longitudinal wave speed [m/s]	5850	5632	218	3.7%	—
Two-way transit time, $h = 0.5$ µm [ps]	170.9	177.6	6.6	3.9%	—

10.3 Thermal measurements in steel cylinders

A direct comparison of computed and measured temperature histories in a steel cylinder would complement the comparisons above. Fakir et al. (2018) heated AISI 4340 cylinders of 15 mm diameter, rotating at 5000 rpm, with a

stationary 1 mm laser spot of 2–3 kW for 1.5 s, recorded surface temperatures with a pyrometer and measured the hardness profiles; they validated a finite-difference heat-conduction model against COMSOL simulations, with the absorption coefficient (about 0.67) calibrated on the pyrometer data. These experiments cannot be reproduced by the present model: the surface temperature reaches 1400–1500 K, so that $|\theta/T_0| \approx 4$ instead of $|\theta/T_0| \ll 1$; the steel austenitizes and, at 3 kW, melts near the surface; the thermal properties vary strongly with temperature; and the rotating heat source is not axisymmetric with respect to the cylinder axis. In addition, the temperature histories are reported only graphically. A comparison of temperature histories (a Fig. 15) was therefore not made, because it could not be carried out under the physical conditions assumed by the model. A suitable benchmark would be a 4340 cylinder heated over part of its end face by a few kelvin, with thermocouples or infrared thermography on the lateral face and strain gauges near the clamped base.

10.4 Calibration and identifiability of the fractional-memory parameters

Table 11 lists the status of every parameter. The elastic and thermal constants are handbook values of measured properties; the longitudinal wave speed and the thermoelastic slope have been benchmarked (Section 10.2); the fractional order, the memory interval, the kernel and the relaxation constants are assumed.

The tensile-bar data discriminate between heat laws. With the illustrative FMDD parameters of Table 7 ($\tau_v = 9.4 \times 10^{-14}$ s, $\beta = 0.5$) the gauge length exchanges heat with the grips almost instantaneously, and the predicted temperature change is practically zero (Fig. 14(a)), contrary to both measurements. Fig. 14(b) shows the fraction of the isentropic temperature change retained after 2 s as a function of the dimensional memory time. The measured loading slope implies a retained fraction of at least 0.59, and other heat losses can only lower the measured value. The FMDD law is therefore compatible with the measurement only if $\tau_v \geq 5.4 \times 10^{-7}$ s for $\beta = 0.25$, $\tau_v \geq 6.9 \times 10^{-4}$ s for $\beta = 0.5$ and $\tau_v \geq 5.2 \times 10^{-3}$ s for $\beta = 0.70$, that is, 7 to 11 orders of magnitude above the illustrative value. For $\beta = 0.70$ the retained fraction is not monotonic in τ_v, because the nearly wave-like heat transport carries a thermal pulse from the grips into the gauge length.

Whether the data can also *identify* τ_v was tested by a calibration–validation split. Under the hypothesis that the whole deficit of the loading slope is caused by the heat law, τ_v was calibrated on the loading data, giving 9.9×10^{-7} s, 9.2×10^{-4} s and 6.2×10^{-3} s for $\beta = 0.25$, 0.5 and 0.70. The calibrated models were then used to predict the independent unloading measurement. For an unloading time of 5 µs to 1 ms, all calibrated models, and also the Biot law, predict -1.014 K/GPa, in agreement with the measured -1.2 ± 0.3 K/GPa, because the thermal disturbance from the grips penetrates less than a millimetre in that time. The unloading data are therefore equally consistent with the hypothesis that the deficit is due to the heat law and with the explanation of Burns et al. (2025) that it is due to heat exchange with the fixtures. The memory time is bounded from below but not identifiable from these data, and the parameters β, τ_v, ω and the kernel remain illustrative model parameters.

The sensitivity of the lower bounds was examined for the parameters of the identification. Halving or doubling the ratio ω/τ_v changes the bounds by less than 0.2%, so the memory interval is not constrained by these data. Moving the isothermal reservoirs from $\ell = 40$ mm to 60 mm, to represent the shoulders of the specimen, lowers the bounds by factors of 44, 6.6 and 3.8 for $\beta = 0.25$, 0.5 and 0.70, and using the temperature at the midpoint instead of the extensometer mean lowers them by factors of 1.4 to 2.5. The bounds are therefore order-of-magnitude estimates, but every variant remains at least 5 orders of magnitude above the illustrative value of Table 7.

Table 11 Material and model parameters and their experimental status

Parameter	Value	Unit	Source	Status
Density ρ	7850	kg/m^3	MakeItFrom.com (2026)	Measured (handbook)
Young's modulus E	190	GPa	MakeItFrom.com (2026)	Measured (handbook); 205 GPa implied by the measured wave speed
Poisson's ratio ν	0.29	—	MakeItFrom.com (2026)	Measured (handbook)
Thermal conductivity k	44	W/(m K)	MakeItFrom.com (2026)	Measured (handbook)
Specific heat C_E	470	J/(kg K)	MakeItFrom.com (2026)	Measured (handbook)
Thermal expansion α_T	13×10^{-6}	K^{-1}	MakeItFrom.com (2026)	Measured (handbook)
Coupling $\alpha_T T_0/(\rho C_\sigma)$	1.014	K/GPa	Eq. (54)	Benchmarked: unloading data, error 15%
Wave speed c_0	5632	m/s	Table 7 constants	Benchmarked: measured 5850 m/s, error 3.7%
Fractional order β	0.25–0.70	—	Assumed; Eq. (12) bound	Assumed, not identifiable from available data
Memory time τ_v	9.4×10^{-14}	s	Assumed (Table 7)	Assumed; inconsistent with tensile data at structural scale; lower bound 5.4×10^{-7}–5.2×10^{-3} s
Memory interval ω, kernel	$0.8\tau_v$, quadratic	s	Assumed	Assumed, insensitive to available data
Relaxation constants A, a, b_v	0.1, 0.5, 0.5	—	Assumed	Assumed, not calibrated
Surface temperature rise ΔT_0	5	K	Assumed loading	Assumed

10.5 Sources of experimental discrepancies

The comparisons contain several sources of discrepancy that are not related to the heat transport law. (i) *Heat exchange with the test fixtures.* Burns et al. (2025) attributed the low loading slope to heat exchange with the threaded ends, the fixtures and the machine, and found that the sum of the cooling and heating contributions is about 95% of the isentropic value; the present model represents this exchange only by isothermal reservoirs at the ends of the gauge length. (ii) *Material constants.* The constants used by Burns et al. ($\alpha_T = 12.3 \times 10^{-6}$ K^{-1}, $c_p = 475$ J/(kg K)) give an isentropic slope of -0.963 K/GPa, 5.3% below the value from Table 7, so the handbook data alone introduce an uncertainty of about 5%. (iii) *Microstructure.* The ultrasonic velocity of 4340 steel depends on the heat treatment (El Rayes et al. 2015), whereas the model uses one set of room-temperature handbook constants. (iv) *Measurement.* The infrared temperatures depend on the emissivity of the painted surface, and the unloading measurement occurs after plastic deformation and fracture, which the linear model does not represent. (v) *Idealized loading.* Uniform uniaxial stress is assumed over the gauge length, whereas the stress decreases in the shoulders.

10.6 Limitations of the present model

The formulation is linear, with temperature-independent properties, and is restricted to small temperature rises; it excludes plasticity, phase transformations and the temperature dependence that dominate laser processing (Section 10.3). The heat law (8) contains no Fourier term. At the structural scale this produces thermal transients far faster than Fourier conduction with the illustrative parameters (Case I) and requires memory times many orders of magnitude larger to agree with the tensile-bar data (Section 10.4). A physically calibrated model may therefore require an additional Fourier contribution, as in the Green–Naghdi type III theory; such a model must be derived and verified separately and has not been used here. At the sub-micron scale (Case II), a 0.5 μm cylinder is smaller than the typical grain size of quenched and tempered or normalized 4340 steel, so that an isotropic continuum with polycrystalline constants is an approximation, and electron–phonon nonequilibrium is not represented by a single-temperature model (Singh 2025). The reference geometry of the nondimensional study, $R_0 = h = 1$, corresponds to 2.12 nm and lies at the limit of continuum mechanics; those results are parametric. Table 12 classifies the results of the study accordingly.

Table 12 Status of the results

Category	Results
Experimental benchmarking	Thermoelastic coupling (Eq. (54)) against tensile-bar measurements on AISI 4340; longitudinal wave speed and transit times against the measured ultrasonic velocity; lower bounds on the FMDD memory time
Numerical verification	Biot, Lord–Shulman, Green–Naghdi II and fractional–memory–viscoelastic limits against finite differences (Table 3); two-dimensional modes against Chebyshev collocation; convergence and boundary residuals (Tables 4, 5); Case I against the exact quasi-static solution (Table 8); tensile-bar inversion against the exact series
Theoretical predictions	Effects of the fractional order, kernel, relaxation and heated edge (Figs. 4–11); tensile stresses near the clamped base; Case II penetration depths, stresses and surface displacement (Fig. 13); all FMDD and viscoelastic fields with the parameters of Table 7; design maps under rapid heating (Fig. 15, Table 13)

11 Design implications for AISI 4340 components

The results of Sections 9 and 10 are interpreted here in terms of the quantities used in design: the peak equivalent (von Mises) stress, its location, and the temperature rise that a component can sustain without yielding. The yield strength of AISI 4340 ranges from 470 MPa (annealed) to 1150 MPa (quenched and tempered), and its fatigue strength from 330 to 740 MPa (MakeItFrom.com 2026). Because the problem is linear, a stress σ/θ_0 obtained for the nondimensional surface temperature corresponds to $\gamma\,\Delta T_0\,\sigma/\theta_0$ in physical units, with $\gamma = 5.88$ MPa/K for the constants of Table 7, and the allowable temperature rise is

$$\Delta T_Y = \frac{\sigma_Y}{\gamma\,\sigma_{eq,\max}/\theta_0}, \qquad \sigma_{eq} = \left\{\tfrac{1}{2}\left[(\sigma_{rr}-\sigma_{\varphi\varphi})^2 + (\sigma_{\varphi\varphi}-\sigma_{zz})^2 + (\sigma_{zz}-\sigma_{rr})^2\right] + 3\sigma_{rz}^2\right\}^{1/2}. \tag{56}$$

11.1 Slow heating at the structural scale

At the structural scale the response is quasi-static (Case I), and the Biot limit of the model has been verified against the exact solution (Table 8) and its coupling term benchmarked against measurements (Section 10.2). Near the heated face the stress state is then $\sigma_{rr} = \sigma_{\varphi\varphi} = -2\hat{\mu}\gamma\theta$, $\sigma_{zz} = 0$, so that $\sigma_{eq} = 2\hat{\mu}\gamma\theta = E\alpha_T\theta/(1-\nu)$, that is 3.48 MPa per kelvin. Eq. (56) then gives the classical limit $\Delta T_Y = (1-\nu)\sigma_Y/(E\alpha_T)$, which is 135–331 K for the yield-strength range of AISI 4340 and 95–213 K if the fatigue strength is used for repeated heating. These values exceed the small-temperature range of the linear theory ($|\theta/T_0| \ll 1$); above a temperature rise of a few tens of kelvins they should be regarded as first estimates, to be refined with temperature-dependent properties and, for quenched and tempered steel, checked against the tempering temperature. The diffusion time $h^2\rho C_E/k$ (33.5 s for $h = 20$ mm) separates slow heating, for which this quasi-static limit applies, from rapid heating, for which transient gradients and stress waves must be considered.

11.2 Dynamic amplification under rapid localized heating

For rapid localized heating, the peak equivalent stress was computed over the whole cylinder and over the time window $0 < t \le 2.4$ for aspect ratios $h/R_0 = 0.5$–3 and heated radii $b/R_0 = 0.25$–1 (smoothed edge $\delta = 0.02$ for $b < R_0$), with the FMDD law of Table 7 and with the Biot law. Fig. 15(a) shows the peak normalized by the quasi-static value $2\hat{\mu}\theta_0$, i.e. a dynamic amplification factor, and Fig. 15(b) the corresponding allowable temperature rise for $\sigma_Y = 470$ MPa; Table 13 gives the values and locations for $b/R_0 = 0.5$. Increasing the number of Dini modes and Laplace terms changed the peaks by less than 2%, and sampling the time at intervals of 0.15 underestimates the early surface peaks of tall cylinders by up to 3%. These maps are computed for the reference geometry of the nondimensional study ($R_0 = 1$), at which thermal and elastic time scales are comparable; they quantify trends under rapid heating and are not dimensional predictions for macroscopic parts (Section 10.6).

Three regimes can be distinguished. (i) For a small heated spot ($b/R_0 = 0.25$), the peak occurs on the heated face shortly after heating, is nearly independent of the height, and remains below the quasi-static value (factor 0.85–0.95); the allowable temperature rise is 142–159 K for $\sigma_Y = 470$ MPa. (ii) For short cylinders ($h/R_0 \le 1$) heated over a large part of the face ($b/R_0 \ge 0.5$), the amplification reaches 1.2–2.1, and the peak moves into the interior or, for $h/R_0 = 1$, to the clamped base after the reflection of the stress wave (Table 13); the allowable temperature rise falls to 65–111 K, down to about half of the quasi-static limit. (iii) For taller cylinders ($h/R_0 \ge 1.5$) the amplification decreases towards 1, except for large heated radii ($b/R_0 \ge 0.75$), for which the stress wave and its reflection still raise the peak by up to 50% within the time window. The FMDD law gives peaks between 4% lower and 29% higher than the Biot law, so that the uncertainty of the heat-transport law should be covered by the safety factor when rapid heating is expected.

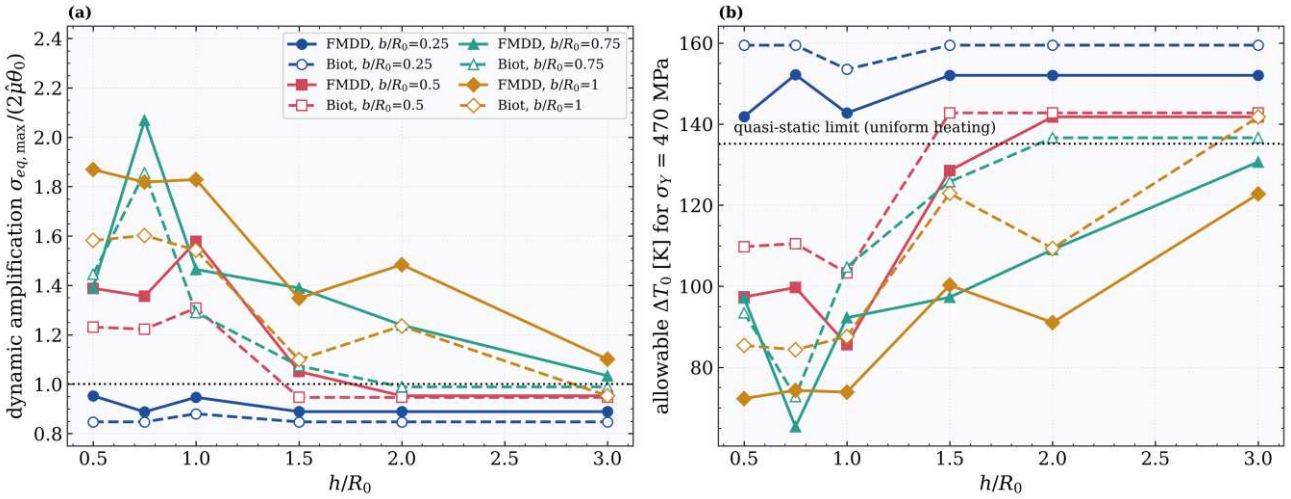


Fig. 15 Design maps for AISI 4340 cylinders under rapid localized heating, FMDD law (filled markers) and Biot law (open markers): (a) peak von Mises stress over the cylinder and over $0 < t \le 2.4$, normalized by the quasi-static value $2\hat{\mu}\theta_0$; (b) allowable surface temperature rise for a yield strength of 470 MPa, Eq. (56); the dotted line marks the quasi-static limit $(1-\nu)\sigma_Y/(E\alpha_T)$

Table 13 Design values for AISI 4340 cylinders ($b/R_0 = 0.5$, $\delta = 0.02$): peak von Mises stress over the cylinder and over $0 < t \le 2.4$, its location, peak axial tension and allowable temperature rise $\Delta T_Y = \sigma_Y/(\gamma\,\sigma_{eq,\max})$ for $\sigma_Y = 470$ and 1150 MPa

h/R_0	$\sigma_{eq,\max}/\theta_0$ FMDD	$\sigma_{eq,\max}/\theta_0$ Biot	Location (r,z,t), FMDD	$\sigma_{zz,\max}/\theta_0$ FMDD	ΔT_Y [K], FMDD	ΔT_Y [K], Biot
0.5	0.821	0.728	(0.00, 0.20, 1.20)	1.292	97–238	110–269
0.75	0.802	0.723	(0.00, 0.07, 1.50)	1.254	100–244	111–270
1	0.934	0.774	(0.13, 1.00, 1.05)	1.580	86–209	103–253
1.5	0.622	0.560	(0.00, 1.10, 1.95)	0.908	129–314	143–349
2	0.564	0.560	(0.00, 0.00, 0.15)	0.830	142–347	143–349
3	0.564	0.560	(0.00, 0.00, 0.15)	0.763	142–347	143–349

11.3 Design recommendations

(1) For slow heating of AISI 4340 parts, the quasi-static limit $\Delta T_Y = (1-\nu)\sigma_Y/(E\alpha_T)$, benchmarked through its coupling term, provides the allowable temperature rise. (2) For rapid heating of short cylinders over a large part of an end face, a dynamic amplification of up to about 2 should be assumed, and the clamped base should be included among the critical sections, for example by using a fillet or a less rigid support. (3) For small heated spots the heated surface remains the critical location, and the quasi-static limit is conservative. (4) Because the predicted peaks depend on the heat-transport law by up to about 30%, and because the fractional-memory parameters of AISI 4340 are not yet identified (Section 10.4), dimensional predictions for a specific component should be made with the Biot law at structural scales and with calibrated parameters for ultrafast heating.

12 Conclusions

A fractional Green–Naghdi thermoviscoelastic formulation with a memory-dependent derivative has been obtained by replacing the fractional heat equation of Hendy et al. (2019), and it has been solved for a finite cylinder with the constants of AISI 4340 alloy steel by the state-space approach. The principal findings of the nondimensional parametric analysis, the two case studies expressed in physical units, the comparison with published measurements and the design interpretation are summarized below.

1. The formulation contains the Biot, Lord–Shulman, Green–Naghdi II and memory-dependent models as limiting cases. Its heat law enters the transformed solution only through $\Lambda(s) = \tau_v^{\beta} s^{\beta+1}[1+G(s)]$.
1. Harmonic passivity of the uncoupled heat law bounds the fractional order: $\beta \le 2/3$ for the constant kernel, 0.721 for the linear kernel and 0.742 for the quadratic kernel. All results were computed within these bounds; the bounds do not establish stability of the full coupled system.
2. Retaining both exponential branches of the matrix exponential gives an analytical, numerically stable transform-domain solution for a body of finite height that represents reflections from the clamped base.
3. The solution agrees with independent time-domain finite-difference solutions in the Biot, Lord–Shulman, Green–Naghdi II and fractional–memory–viscoelastic one-dimensional cases, with a Chebyshev collocation solution of the transformed two-dimensional modes, and it converges with the number of Dini modes and Laplace terms (Tables 3–5).

4. Within the admissible range, increasing the fractional order confines the thermal disturbance and increases the compressive stresses behind the elastic front; the memory kernel and the viscoelastic relaxation modify the near-surface temperature and stresses.
5. The hoop stress changes sharply across the edge of the heated disk; this change converges for smoothed heating profiles but depends on the edge width, whereas some stresses near the idealized sharp edge do not converge.
6. For the stated constraints, the model predicts tensile stresses near the clamped base after the reflection of the elastic front; this is a computational prediction that a half-space model cannot represent.
7. Two case studies in physical units have been examined using the material constants of AISI 4340 steel. At the structural scale, the classical Biot solution agrees with the exact quasi-static temperature and stress distributions; this comparison verifies the numerical implementation in the classical limit. The fractional-memory model predicts substantially faster thermal transients when illustrative sub-picosecond parameters are used at the same scale; these results demonstrate the need for physical calibration before structural applications. At the sub-micron scale, the different heat transport laws predict differences in quantities that may be experimentally measured, namely thermal penetration, transient stresses and surface motion. These predictions provide potential targets for experimental investigation, but do not constitute experimental validation of the fractional model.
8. Experimental benchmarking against published measurements on AISI 4340 supports the thermoelastic coupling and the elastic wave speed of the model: the predicted isentropic coefficient, -1.014 K/GPa, agrees with the measured unloading value of -1.2 ± 0.3 K/GPa (relative error 15%), and the predicted longitudinal wave speed is 3.7% below the measured ultrasonic velocity. These comparisons test the classical thermoelastic part of the model; they do not validate the fractional-memory heat law.
9. The same tensile-bar data exclude the illustrative fractional-memory parameters at the structural scale and require memory times of at least 5.4×10^{-7} s, 6.9×10^{-4} s and 5.2×10^{-3} s for $\beta = 0.25$, 0.5 and 0.70 under the stated idealization of the grips. A calibration–validation test shows that the memory time is bounded but not identifiable from these data, and the memory interval is insensitive to them. Laser-hardening temperature data for 4340 cylinders violate the small-temperature, single-phase assumptions of the model and were not used for validation. Identification of the fractional order, memory kernel and relaxation constants for this steel, for example with the low-temperature cylinder test outlined in Section 10.3, remains the main task for future experiments.
10. A design interpretation gives the allowable temperature rise of AISI 4340 parts under slow heating as $(1-\nu)\sigma_Y/(E\alpha_T)$, i.e. 135–331 K over the yield-strength range of the steel. Under rapid localized heating of short cylinders ($h/R_0 \le 1$, $b/R_0 \ge 0.5$) the peak von Mises stress is amplified by 1.2–2.1 relative to the quasi-static value, the clamped base can become the critical section, and the heat-transport law changes the peak by up to 29%; these maps are parametric results at the reference scale of the nondimensional study.

Nomenclature

Symbol	Meaning
$\lambda, \mu;\ K$	Lamé constants; bulk modulus
$\rho,\ C_E,\ k$	Density, specific heat, thermal conductivity
C_σ	Specific heat at constant stress, $C_E + 3\alpha_T\gamma T_0/\rho$
$\alpha_T;\ \gamma$	Thermal expansion coefficient; $(3\lambda + 2\mu)\alpha_T$
$T_0;\ \theta$	Reference temperature; temperature increment
$\sigma_{ij},\ \varepsilon_{ij}$	Stress and strain tensors
$S_{ij},\ e_{ij};\ e$	Stress and strain deviators; dilatation
u_r, u_z	Displacement components
$\hat{R}(t);\ A, a, b$	Relaxation modulus and its constants
$\tau_v;\ \beta$	Green–Naghdi parameter; fractional order
$\omega;\ K(t-\xi)$	Time-delay and kernel of the MDD
$c_0;\ \eta_0$	Longitudinal wave speed; $\rho C_E/k$
ε	Thermoelastic coupling parameter
R_0, h, b	Radius, height, heated radius
$\theta_0;\ \Delta T_0$	Nondimensional and physical surface temperature rise
$s;\ \xi_n$	Laplace parameter; roots of $J_1(\xi_n R_0) = 0$

Acknowledgements

The authors acknowledge the support provided by the Deanship of Scientific Research at Northern Border University, Arar, Saudi Arabia.

Funding

This research was supported by the Deanship of Scientific Research at Northern Border University under Grant No. NBU-FFR-2026-1695-07.

Disclosure statement

No potential conflict of interest was reported by the authors.

Data availability statement

All data generated in this study are contained in the article. The experimental values used for benchmarking are taken from the cited publications (Burns et al. 2025; Evident Scientific 2026). The Python codes that reproduce all figures and tables, including the state-space solver, the independent finite-difference solvers, the Chebyshev collocation check and the benchmarking and design scripts, are available from the corresponding author on reasonable request.

References

Abbas, I.A., Kumar, R.:2D deformation in initially stressed thermoelastic half-space with voids. Steel Compos. Struct. **20**(5), 1103-1117 (2016). doi:10.12989/scs.2016.20.5.1103.

Aldawody, D.A., Hendy, M.H., Ezzat, M.A.: On dual-phase-lag magneto-thermo-viscoelasticity theory with memory-dependent derivative. Microsyst. Technol. 25(8), 2915-2929 (2018). doi:10.1007/s00542-018-4194-6.

Bahar, L.Y., Hetnarski, R.B.: State space approach to thermoelasticity. J. Therm. Stresses. 1(1), 135-145(1978).doi:10.1080/01495737808926936.

Biot, M.A.: Thermoelasticity and irreversible thermodynamics. J. Appl. Phys. 27(3), 240-253(1956). doi:10.1063/1.1722351.

Burns, S. J., Pratt, C. E., Carrock, J., Gagnon, J. –P., Sefkow, A. B.: Experimental investigation of Lord Kelvin's isentropic thermoelastic cooling and heating expression for tensile bars in two engineering alloys. Philosoph. Magaz. 105 (2025). doi:10.1080/14786435.2024.2390013.

Chandrasekharaiah, D.S.: Hyperbolic thermoelasticity: a review of recent literature. Appl. Mech. Rev. 51(12), 705-729 (1998). doi:10.1115/1.3098984.

El-Karamany, A.S., Ezzat, M.A.: Discontinuities in generalized thermo-viscoelasticity under four theories. J. Therm. Stresses. 27(12), 1187-1212(2004). doi:10.1080/014957390523598.

El Rayes, M. M., El-Danaf, E. A., Almajid, A. A.: Ultrasonic characterization of heat-treatment effects on SAE-1040 and -4340 steels. J. Mater. Process. Techno. 216,188–198(2015). doi:10.1016/j.jmatprotec.2014.09.005.

Evident Scientific.: Material sound velocities. Accessed October (2026). https://ims.evidentscientific.com/en/learn/ndt-tutorials/thickness-gauge/appendices-velocities.

Ezzat, M.A.: State space approach to solids and fluids. Can. J. Phys. 86(11), 1241-1250(2008). doi:10.1139/p08-069.

Ezzat, M.A.: Thermoelectric MHD with modified Fourier's law. Int. J. Therm. Sci. 50(4), 449-455(2011). doi:10.1016/j.ijthermalsci.2010.11.005.

Ezzat, M.A., El-Bary, A.A.: Fractional magneto-thermoelastic materials with phase-lag Green-Naghdi theories. Steel Compos. Struct. 24(3), 297-307(2017). doi:10.12989/scs.2017.24.3.297.

Ezzat, M.A., El-Karamany, A.S.: The uniqueness and reciprocity theorems for generalized thermov-iscoelasticity with two relaxation times. Int. J. Eng. Sci. 40(11), 1275-1284(2002). doi:10.1016/S0020-7225(01)00099-4.

Ezzat, M.A., El-Karamany, A.S.: On uniqueness and reciprocity theorems for generalized thermo-viscoelasticity with thermal relaxation. Can. J. Phys., 81(6), 823-833(2003). doi:10.1139/p03-070.

Ezzat, M.A., El-Karamany, A.S.: Fractional thermoelectric viscoelastic materials. J. Appl. Polym. Sci. 124(3), 2187-2199(2012). doi:10.1002/app.35243.

Ezzat, M.A., El-Karamany, A.S., El-Bary, A.A.: Generalized thermo-viscoelasticity with memory-dependent derivatives. Int. J. Mech. Sci. 89, 470-475(2014). doi:10.1016/j.ijmecsci.2014.10.006.

Ezzat, M.A., El-Karamany, A.S., El-Bary, A.A.: On thermo-viscoelasticity with variable thermal conductivity and fractional-order heat transfer. Int. J. Thermophys. 36(7), 1684-1697(2015). doi:10.1007/s10765-015-1873-8.

Ezzat, M.A., El-Karamany, A.S., El-Bary, A.A.: Modeling of memory-dependent derivative in generalized thermoelasticity. Eur. Phys. J. Plus. **131**, 372(2016). doi:10.1140/epjp/i2016-16372-3.

Ezzat, M.A., El-Karamany, A.S., Samaan, A.A.: State-space formulation to generalized thermoviscoelasticity with thermal relaxation. J. Therm. Stresses. 24(9), 823-846(2001). doi:10.1080/014957301750379612.

Ezzat, M.A., Othman, M.I., El-Karamany, A.S.: State space approach to generalized thermo-viscoelasticity with two relaxation times. Int. J. Eng. Sci. 40(3), 283-302(2002) . doi:10.1016/S0020-7225(01)00045-3.

Fakir, R., Barka, N., Brousseau, J.: Case study of laser hardening process applied to 4340 steel cylindrical specimens using simulation and experimental validation. Case Studi. Therm. Eng. 11,15–25 (2018). doi:10.1016/j.csite.2017.12.002.

Green, A.E., Lindsay, K.A.: Thermoelasticity. J. Elast. 2(1), 1-7(1972). doi:10.1007/BF00045689.

Green, A.E., Naghdi, P.M.: A re-examination of the basic postulates of thermomechanics. Proc. R. Soc. Lond. A. 432(1885), 171-194(1991). doi:10.1098/rspa.1991.0012.

Green, A.E., Naghdi, P.M.: On undamped heat waves in an elastic solid. J. Therm. Stresses. 15(2), 253-264(1992). doi:10.1080/01495739208946136.

Green, A.E., Naghdi, P.M.: Thermoelasticity without energy dissipation. J. Elast. 31(3), 189-208(1993). doi:10.1007/BF00044969.

Gross, B.: Mathematical Structure of the Theories of Viscoelasticity, Hermann, Paris, France (1953).

Hendy, M.H., Amin, M.M., Ezzat, M.A.: Magneto-electric interactions without energy dissipation for a fractional thermoelastic spherical cavity. Microsys. Technol. 24(7), 2895-2903(2018). doi:10.1007/s00542-017-3643-y.

Hendy, M.H., Amin, M.M., Ezzat, M.A.: Two-dimensional problem for thermoviscoelastic materials with fractional order heat transfer. J. Therm. Stresses. 42(10), 1298-1315(2019). doi:10.1080/01495739.2019.1623734.

Honig, G. and Hirdes, U.: A method for the numerical inversion of Laplace transforms. J. Comput. Appl. Math. 10(1), 113-132(1984). doi:10.1016/0377-0427(84)90075-X.

Lata, P., Kumar, R., Sharma, N.: Plane waves in an anisotropic Thermoelastic. Steel Compos. Struct. 22(3), 567-587(2016). doi:10.12989/scs.2016.22.3.567.

Lord, H.W., Shulman, Y.: A generalized dynamical theory of thermoelasticity. J. Mech. Phys. Solids. 15(5), 299-309 (1967). doi:10.1016/0022-5096(67)90024-5.

MakeItFrom.com. 2026. SAE-AISI 4340 (SNCM439, G43400) Ni-Cr-Mo steel. Accessed October (2026). https://www.makeitfrom.com/material-properties/SAE-AISI-4340-SNCM439-G43400-Ni-Cr-Mo-Steel.

Povstenko, Y.Z.: Fractional heat conduction equation and associated thermal stress. J. Therm. Stresses. 28(1), 83-102(2005).doi:10.1080/014957390523741.

SAE SAE J404.: Chemical Compositions of SAE Alloy Steels, SAE Int., Warrendale, PA, USA (2009).

Sherief, H.H.: State space approach to thermoelasticity with two relaxation times. Int. J. Eng. Sci. 31(8), 1177-1189(1993). doi:10.1016/0020-7225(93)90091-8.

Sherief, H.H., El-Sayed, A.M.A., Abd El-Latief, A.M.: Fractional order theory of thermoelasticity. Int. J. Solids Struct. 47(2), 269-275 (2010). doi:10.1016/j.ijsolstr.2009.09.034.

Sherief, H.H., Hamza, F.A., Abd El-Latief, A.M.:2D problem for a half-space in the generalized theory of thermo-viscoelasticity. Mech. Time-Depend. Mater. 19(4), 557-568(2015). doi:10.1007/s11043-015-9278-4.

Singh, N.: Hot electron relaxation: A review of the two- temperature model for ultrafast non-equilibrium phenomena in metals. APL Quantum, 2(2), 021502(2025). doi:10.1063/5.0262933.

Thomsen, C., Grahn, H.T., Maris, H.J., Tauc, J.: Surface generation and detection of phonons by picosecond light pulses. Phys. Rev. B, 34(6), 4129-4138(1986). doi:10.1103/PhysRevB.34.4129.

Tschoegl, N.W.: Time dependence in material properties: an overview. Mech. Time-Depend. Mater. 1(1), 3-31(1997). doi:10.1023/A:1009748023394.

Wang, J.L., Li, H.F. Surpassing the fractional derivative: concept of the memory-dependent derivative. Comput. Math. Appl. 62(3), 1562-1567(2011). doi:10.1016/j.camwa.2011.04.028.

Youssef, H.M.: Theory of fractional order generalized thermoelasticity. J. Heat Transfer. 132(6), 061301(2010). doi:10.1115/1.4000705.

Yu, Y.J., Hu, W., Tian, X.G.: A novel generalized thermoelasticity model based on memory-dependent derivative. Int. J. Eng. Sci. 81, 123-134(2014).. doi:10.1016/j.ijengsci.2014.04.014.